



# Baryon Resonance Extraction from $\pi N$ Data using a Unitary Multichannel Model

T.P. Vrana\* and S.A. Dytman†

*Department of Physics and Astronomy, University of Pittsburgh, Pittsburgh, PA 15260*

T.-S. H. Lee

*Physics Division, Argonne National Laboratory, Argonne, IL 60439*

(July 12, 1999)

## Abstract

A unitary multi-channel approach, first developed by the Carnegie-Mellon-Berkeley group, is applied to extract the pole positions, masses, and partial decay widths of nucleon resonances from the partial wave amplitudes for the transitions from  $\pi N$  to eight possible final baryon-meson states. Results of single energy analyses of the VPI group using the most current database are used in this analysis. A proper treatment of threshold effects and channel coupling within the unitarity constraint is shown to be crucial in extracting resonant parameters, especially for the resonance states, such as  $S_{11}(1535)$ , which have decay thresholds very close to the resonance pole position. The extracted masses and partial decay widths of baryon resonances up to about 2 GeV mass are listed and compared with the results from previous analyses. In many cases, the new results agree with previous analyses. However, some significant differences, in particular for the resonances that are weakly excited

---

\*Present Address: Fisher Scientific Corp., Pittsburgh, PA

†email:dytman+@pitt.edu; phone:412-624-9244; fax:412-624-9163

in  $\pi N$  reactions, are found.

13.30.-a,13.75.Gx,13.30.Eg,14.20.-c

## Contents

<b>I</b>	<b>Introduction</b>	<b>5</b>
<b>II</b>	<b>The CMB Unitary Multi-channel Model</b>	<b>11</b>
	A Representation of 3-body final states . . . . .	11
	B Model details . . . . .	12
	C Resonance parameter extraction . . . . .	16
	D Relationship to other models . . . . .	20
<b>III</b>	<b>Database</b>	<b>22</b>
	A $\pi N$ elastic data . . . . .	23
	B $\pi N \rightarrow \pi\pi N$ data . . . . .	24
	C Description of the $\pi N \rightarrow \eta N$ Analysis . . . . .	25
<b>IV</b>	<b>Illustrative Examples- <math>P_{33}</math> and <math>S_{11}</math> Partial Waves</b>	<b>26</b>
	A Single Channel-Single Resonance Case . . . . .	27
	B Two Channel- Two Resonance Case . . . . .	28
	C Cusp structure in the $S_{11}$ partial wave . . . . .	31
	D Model Dependence in Analysis of the $S_{11}$ partial wave . . . . .	32
	E Elastic Data Dependence . . . . .	35
	F The nonresonant amplitude . . . . .	35
<b>V</b>	<b>Results and Discussion</b>	<b>36</b>
	A Details of Fitting . . . . .	37
	B General Results . . . . .	40
	C Detailed Discussion - $D_{15}$ , $D_{13}$ , and $S_{11}$ Partial Waves . . . . .	44
	D Observables . . . . .	47
<b>VI</b>	<b>Conclusions</b>	<b>48</b>

## I. INTRODUCTION

The interest in the study of baryon resonances began many years ago and led to the important discovery of SU(3) symmetry. Although many states were discovered, the quality and scope of the data limited the analyses. Interest has grown significantly in the last few years because of the prospects for new data of high quality at facilities such as the Thomas Jefferson National Accelerator Facility, the Bonn synchrotron, and Brookhaven National Laboratory. These are excited states of the nucleon with excitation energy of about 0.3 - 1 GeV. Since most of these states were discovered in amplitude analyses of  $\pi N \rightarrow \pi N$  scattering data, they are labeled by the approximate mass and the  $\pi N$  quantum numbers: the relative orbital angular momentum L, the total isospin T, and the total angular momentum J. For example, the  $D_{13}(1520)$  resonance has a mass of about 1520 MeV, isospin T=1/2, total angular momentum J=3/2, and decays into a L=2  $\pi N$  state. Information about the various baryon resonances is evaluated and tabulated in biennial publications of the Particle Data Group [1]. In their 1998 publication, they list about 20  $N^*$  (T=1/2) and 20  $\Delta$  (T=3/2) states. Some states are well established in the data and most analyses agree on their properties. On the other hand, some very large discrepancies exist between different analyses. For example, the extracted full widths for the  $S_{11}(1535)$  state (A 4\* state of PDG [1]) are 66 MeV [2],  $120 \pm 20$  MeV [3],  $151 \pm 27$  MeV [4], 151-198 MeV [5], and  $270 \pm 50$  MeV [6]. This state has a number of striking properties - unusual strong decay width to  $\eta N$  [1] and an unusually flat transition form factor [7] - that have made it a very interesting state to understand. Although there are a number of strongly excited states (rated 4\* or 3\* by PDG), there are many weakly excited states whose properties are poorly determined with the existing data. The differences between various amplitude analyses originate for various reasons, including handling of data, method of parameterizing nonresonant background, and handling of the many  $N^*$  decay channels. We emphasize the fact that the baryon resonances

always decay into a baryon and one or more of various mesons; the existing analyses differ from each other significantly in the methods used to describe this intrinsically multi-channel problem. Thus, model dependence in extraction of resonance properties makes it difficult to test predictions of theoretical models with existing data. With the new experimental facilities, the situation will soon be greatly improved when more exclusive data for different final states, such as  $\eta N$ ,  $\pi\Delta$ , and  $\rho N$ , become available. One of the major goals of the new experiments is to obtain data for a large number of reactions. This greatly increases the probability of seeing new resonances, e.g. those that couple weakly to the  $\pi N$  channel, but puts significant demands on models to interpret the data consistently. The objective of this work is to revive the multi-channel analysis of partial wave amplitudes into resonance parameters of the Carnegie-Mellon Berkeley (CMB) group. Although this is meant to be a significant step toward a full analysis of all contributing reactions, the equally important problem of extracting partial wave amplitudes from the observables is not considered in this paper.

The baryon resonances (called  $N^*$  states from now on in this paper) extracted from amplitude analyses are thought to be predominantly composed of 3 valence quarks because of the SU(3) symmetry seen in the spectrum of hadrons of low total angular momentum. This notion has been the basis for developing various quark models, ranging from the well-studied Constituent Quark Models [8–11], Chiral Bag Models [12,13], NJL models [14], Soliton models [15], to the most recent Chiral Constituent Quark Models [16]. All of these hadron models are motivated by QCD and are constructed phenomenologically to describe the hadron spectrum in terms of suitable parameterizations of quark confinement mechanisms and quark-quark interactions. With some additional assumptions on the decay mechanisms, these models can use the constructed wave functions to predict the decay widths of the  $N^*$  states. For example, the one-body form of quark currents is used [17,10] in most of the constituent quark models in predicting the  $N^* \rightarrow \gamma N$  decay width. A  ${}^3P_0$  model is assumed in Ref. [18] for creation of  $\bar{q}q$  pairs in the calculation of the decay of an  $N^*$  into nucleons and mesons. The comparison of these predictions with the decay width data, such

as that listed by PDG, is clearly a more detailed test of hadron models. In recent years, lattice QCD calculations have been extended to predict masses of the low lying baryons. [19]. Although the lattice QCD calculations are far superior to the empirical quark models, they are much more difficult to apply to the decay widths. In any case, precise data of resonance parameters such as masses and partial decay widths for various final states are needed to distinguish QCD-inspired hadron models and, ultimately, understand the non-perturbative aspects of QCD.

The determination of resonance parameters is almost always a two-step process. First, phase shift analyses (elastic data) and isobar analyses (inelastic data) are used to separate the cross section and polarization observable data into partial wave amplitudes, often in the form of  $T$  matrices. With a large data set, this determination has less model dependence than the extraction of resonance properties in the second step. If nonresonant effects are small, resonances will show up as counterclockwise rotations in the complex energy plane (Argand diagram) as the energy dependence of these  $T$  matrices is plotted. Partial wave amplitudes have been determined by various groups for elastic scattering and much less often for inelastic scattering. Older elastic scattering analyses of Carnegie-Mellon Berkeley (CMB) [20] and Karlsruhe Helsinki (KH) [3,21] stressed the importance of theoretical constraints such as dispersion relations to ensure the uniqueness of the fit. The data situation has improved significantly since then; the more recent work of the Virginia Polytechnic Institute and State University (commonly called VPI) group is the most visible recent effort [2]. They have regularly updated the data base and attempted to cull out older less viable results. They determine single-energy (also called energy independent)  $T$  matrices for partial waves up to  $L=6$  and satisfy a smaller set of dispersion relations than the earlier work. All these analyses are available in the VPI repository [2]. We use the VPI single-energy elastic partial wave amplitudes from the 1995 analysis (SM95) in this work. At the same time, we recognize the point made by Höhler [22] that this analysis is not as well constrained as the older analyses. We use the single-energy solutions rather than the more debatable smoothed solutions.

The second step is to extract the resonance parameters from the partial wave amplitudes.

In a simple picture, each transition amplitude in a  $\pi N$  reaction would be parameterized as the product of the excitation strength of the incident channel to a given resonance and the decay strength of the resonance into the allowed final states with a resonance propagator for the intermediate state. However, this s-channel resonant mechanism is far from complete since the u-channel and t-channel mechanisms, as implied by crossing symmetry or meson-exchange mechanisms, are known to be important. Thus the parameterization of the amplitude in each partial wave must contain a resonant part and a non-resonant part (called the background term in most of the literature). Furthermore, the threshold effects associated with each decay channel ( $\pi N, \eta N, \gamma N, \pi\Delta, \rho N, \omega N, \pi N^*(1440)$  and others) must be treated correctly within the multi-channel unitarity condition. Thus, resonance extraction requires a significant calculational effort and many articles have presented various ways to proceed in practice. The PDG mostly bases its recommended values for baryons on a few works that study the full resonance region ( $1170 \text{ MeV} < W < 2200 \text{ MeV}$ ). These include older work by the CMB group [6] and the KH group [3], and more recent work by the Kent State University (KSU) group [4], and the VPI group [2]. A very recent work of Feuster and Mosel [5] fits data for  $W < 1900 \text{ MeV}$ . All of these efforts use the data of  $\pi N$  reactions. All maintain unitarity, though the methods employed are quite different. This is reasonable since there is more than one way to implement the unitarity condition. However, these analyses differ significantly from each other in handling the multichannel character of the  $\pi N$  reactions. The CMB and KSU groups use a formalism that allows for many channels, while the KH and VPI groups focus on the  $\pi N$  elastic channel. KH accounts for all inelasticity in absorption parameters and VPI uses a dummy channel to account for all inelasticity. Feuster and Mosel [5] fit elastic scattering and inelastic scattering cross-section data with asymptotic two-body final states directly, and account for all the remaining components of the total inelastic cross section with a dummy inelastic channel. For most strongly excited, isolated states, these five analyses tend to agree within the assigned errors. However, as mentioned above, significant differences between them exist in many cases.

This paper will revive the CMB approach [6] and apply it to extract baryon resonance

parameters from partial wave amplitudes of  $\pi N$  reactions with a large variety of final states. This approach emphasizes the analytic properties of scattering amplitudes in the complex energy-plane that are consistent with the dispersion-relation approach and potential scattering theory. Other methods of handling multi-channel unitarity are through the  $K$ -matrix approximation [2,23,5] and the KSU model [4]. Although the transition amplitude is parameterized in a form similar to these models, there are distinct and important differences. In particular, the threshold for each of eight possible channels is treated correctly with 2- and 3-body unitarity requirements imposed. Thus, resonances can be found as poles in the  $T$ -matrix, a feature missing in most  $K$ -matrix models. Obviously, the CMB approach is most suitable for extracting resonances that are close to inelastic channel thresholds. Although the KSU approach by Manley and Saleski and more recent  $K$  matrix models [5] also account for the structure due to channel openings, their multi-channel parameterization is completely different from the CMB model in realizing the unitarity condition. In the CMB model, dispersion relations are used to guarantee analyticity in the amplitudes. The KSU parameterization is an extension of a  $K$ -matrix formulation. It does not allow the analytic continuation into the complex energy plane, which is required to find the resonance pole. Feuster and Mosel present poles from a speed plot analysis, stating that technical problems associated with their partial wave decomposition prevent direct determination of poles from their  $K$  matrix analysis. There is the additional problem that resonances are associated with poles in the  $T$  matrix rather than the  $K$  matrix.

In the CMB model, the non-resonant t-channel and u-channel mechanisms are simulated by including the transitions to sub-threshold one-particle states with masses below the  $\pi N$  threshold and with the possibility of producing either an attractive or a repulsive potential. Existing models treat these effects in a variety of ways. The empirical method used here is rather different from the polynomial parameterization often used in previous amplitude analyses. The consequence of this difference is very significant in practice since the intrinsic “structure” of the non-resonant term due to the channel opening is built in correctly in the CMB approach, but can be easily missed if the “smoothness” of the background term is the

only criterion. Modern  $K$  matrix methods [5] fit coupling strengths in various diagrams. These have the advantage of fitting fewer parameters than the more empirical approaches and have the correct partial wave decomposition of the diagrams include. The disadvantages include ignoring all off-shell intermediate state scattering and the inability to describe resonances of total angular momentum larger than  $3/2$ .

The CMB approach was published in 1979. Although inelastic data were used in the analysis, the elastic  $\pi N$  scattering data were emphasized. In this work, we follow closely their theoretical approach, making only small changes in the parameterization of the amplitudes. However, we make significant changes in the data set used. We include all  $\pi N \rightarrow \eta N$  data, some of which was unavailable then. (They depended on a separate analysis of backward  $\pi^- p$  elastic scattering and other data [24] to model the eta cusp. This analysis would give different results with the present data set.) We also directly fit  $\pi N \rightarrow \pi\pi N$  inelastic data, represented by the amplitudes determined in the isobar model fit of Manley, Arndt, Goradia, and Teplitz [25]. By including 30 percent more data, the Manley *et al.* inelastic amplitudes are more accurate than those used in the original CMB analysis. Furthermore, we will use the most recent VPI energy independent amplitude [2] as the  $\pi N$  elastic scattering input. This amplitude is significantly different from the one used by the CMB group and is also more accurate than the KH amplitude in the  $S_{11}$  channel, as discussed in Ref. [26]. These differences in the input data make our results for some cases (in particular the  $S_{11}(1535)$  state) significantly different from the CMB values listed in Particle Data Table.

Batinic *et al.* [27] have applied the CMB model to perform an analysis with only 3 channels:  $\pi N$ ,  $\eta N$ , and a dummy channel meant to represent the complex set of  $\pi\pi N$  channels. Their focus is on the dynamics associated with the  $\eta N$  channel. They fit the KH80 [3] energy-independent amplitudes of the  $\pi N$  elastic data and the  $\pi N \rightarrow \eta N$  data. The  $\eta N \rightarrow \eta N$  amplitudes are the predictions of the model. The Brown *et al.* data [28] is the largest body of  $\pi N \rightarrow \eta N$  data in the energy region close to threshold, but it is felt to have significant systematic errors [27,29]. Batinic *et al.* give it a weight 5 times smaller than the other data to deemphasize it. We will use the same  $\pi N \rightarrow \eta N$  data with the same

weights in our analysis. This is an important part of the determination of the parameters associated with the  $S_{11}(1535)$  resonance.

The present work is the first step in an ongoing program to develop a model appropriate for the new generation of data coming from Jefferson Lab and other labs. Although we anticipate further development of the model, the goal of this work is to apply the CMB model in a form very similar to its original implementation. We closely follow the procedures of Ref. [6], but use it to determine the baryon spectrum and decay branching fractions from the modern data. Future publications will address interesting but nontrivial issues such as how to determine the “best” baryon spectrum and how to differentiate between resonance poles, bound state or virtual poles, and poles that have changed Riemann sheet by moving across an inelastic threshold cut to the sheet most directly reached from the physical data.

In section II, we present a detailed account of the CMB multi-channel unitary model. To illustrate the main features of the model, we discuss in section III the examples of an isolated resonance and the 2 resonance-2 channel situation. The full results are presented and discussed in section IV. A summary and outlook are given in section V. A more complete discussion of the methods and results is given in Ref. [30].

## II. THE CMB UNITARY MULTI-CHANNEL MODEL

### A. Representation of 3-body final states

The first step of a multi-channel analysis to determine  $N^*$  parameters is to extract from the  $\pi N \rightarrow \pi\pi N$  data a set of partial-wave amplitudes for the transitions from a  $\pi N$  state to various quasi two-particle channels in which one of the two particles is either a  $\pi N$  or a  $\pi\pi$  resonant state:  $\pi\Delta$ ,  $\rho N$ ,  $\pi N^*(1440)$  and a very broad  $(\pi\pi)_{J=T=0}N$  channel. For convenience, we will use the notation  $\sigma$  to label the S-wave, isoscalar  $\pi\pi$  state. This procedure was introduced by the Carnegie Mellon-Berkeley (CMB) group in the 1970’s. A similar procedure was used later by the Virginia Polytechnic Institute and State University

(VPI) and Kent State University (KSU) groups [25] to obtain partial wave amplitudes from all of the  $\pi N \rightarrow \pi\pi N$  data available in 1984. These amplitudes, called VPI-KSU amplitudes, will be used in this work.

A more precise analysis should start with the original data of  $\pi N \rightarrow \pi\pi N$  reactions. This event data has been stored by the VPI group. The raw  $\pi N \rightarrow \pi\pi N$  data was not received from them in time for the present analysis.

## B. Model details

To extract resonance parameters from VPI-KSU amplitudes, it is necessary to employ a multi-channel formulation of the  $\pi N$  reaction. This is accomplished in the CMB approach by assuming that the transition amplitudes of the  $\pi N$  reaction can be written in the center of mass (c.m.) frame as

$$T_{ab} = \sum_{i,j=1}^N f_a(s) \sqrt{\rho_a(s)} \gamma_{ai} G_{ij}(s) \gamma_{jb} \sqrt{\rho_b(s)} f_b(s) \quad (1)$$

where  $s$  is the total center of mass energy squared, indices  $a, b$  denote the asymptotic channels which can be either a stable two-particle state ( $\pi N, \eta N, K\Lambda, \dots$ ) or a quasi two-particle state ( $\pi\Delta, \rho N \dots$ ). These asymptotic channels are coupled to a set of intermediate states (resonances) denoted by indices  $i, j$ . The scattering matrix defined by Eq. (1) is related to the  $S$ -matrix via  $S = 1 + 2iT$  with  $S^\dagger S = 1$ . Hence we have the following unitarity condition:

$$\Im m(T_{ab}) = \sum_{c=1}^M T_{ac}^* T_{cb} \quad (2)$$

The crucial step of the CMB model is to choose a parameterization of various quantities in Eq. (1) such that Eq. (2) is satisfied. Furthermore, the resulting analytic structure of the scattering amplitudes is consistent with the well-developed dispersion relations for  $\pi N$  elastic scattering and multi-channel potential scattering theories. This is accomplished by using the following prescription. First, it is assumed that the  $i$ th resonance to be found is

identified with the bare particle,  $i$ , with a bare mass squared,  $s_{0,i}$ . The strength constant  $\gamma_{ai}$  and form factor  $f_a(s)$  in Eq. (1) define the decay of the  $i$ th resonance into an asymptotic channel  $a$ . The form factor is defined by

$$f_a(s) = \left( \frac{p_a}{Q_1 + \sqrt{p_a^2 + Q_2^2}} \right)^{l_a} \quad (3)$$

where  $Q_1$  and  $Q_2$  are empirical constants defining how quickly a channel, with orbital angular momentum  $l_a$ , opens up.  $p_a$  is the center of mass momentum for channel  $a$ . In this analysis, we set  $Q_1$  and  $Q_2$  equal to the pion mass. These are the same values as were used by CMB; they chose this parameterization and these values as a result of a study of the best way to model the left-hand cut.

The right-hand or unitarity cut is set through the channel propagators,  $\Im m\phi_a(s) = f_a^2 \rho_a(s)$ . The phase space factor  $\rho_a$  in Eq. (1) is defined by

$$\rho_a = \frac{p_a}{\sqrt{s}} \quad (4)$$

for a stable two-particle state. For quasi two-particle channels,  $\rho_a$  clearly must be defined consistently with the phase space factors used in defining the propagation of this resonant two-body state during the collision, as required by the unitary condition Eq. (2). In the CMB model, this is achieved by assuming that the only interaction during collisions is a vertex interaction which converts intermediate states into asymptotic states. Then the propagator  $G_{ij}$  in Eq. (1) can be graphically depicted in figure 1 and is defined by the Dyson equation:

$$G_{ij} = G_{ij}^0 + G_{il}^0 \Sigma_{lk} G_{kj} \quad (5)$$

Eq. (5) is an iterative equation. A sum over repeated indices is implicit.  $G$ ,  $G_0$ , and  $\Sigma$  all vary with  $s$  and are  $N \times N$  matrices, where  $N$  is the number of intermediate resonant and nonresonant states considered. Each bare intermediate state has a propagator,  $G_0$ , defined by:

$$G_{ij}^0(s) = \frac{\delta_{ij} e_i}{s - s_{0,i}} \quad (6)$$

where  $e_i = +1$  for states that correspond to the resonances that will be fit. To simulate the  $t$ -channel and  $u$ -channel mechanisms, two subthreshold bare states with a mass  $s_{0,i}$  below the  $\pi N$  threshold are introduced. These subthreshold states will simulate an attractive background potential for  $e_i = -1$ , and a repulsive potential for  $e_i = +1$ . In principle, this prescription can simulate any  $t$ - and  $u$ -channel mechanisms if a sufficiently large number of bare states are included. This is well known in potential scattering theory. The actual number of the subthreshold states needed is not intrinsically known. We use two subthreshold states and one state at very high energy for every partial wave. In the original work, CMB [6] found negligible differences between fits using a (smaller) number of subthreshold states and fits using actual potentials that simulate the left-hand cut. They are allowed to couple to  $\pi N$  and  $\eta N$  asymptotic states.

The self-energy,  $\Sigma_{ij}$ , describes the dressing of bare particles by the coupling with two-particle channels, as depicted in figure 2. It therefore must depend on the strengths( $\gamma_{ia}$ 's) and form factors( $f_a$ 's), and is assumed to take the following form

$$\Sigma_{ij}(s) = \sum_{c=1}^M \gamma_{ci} \Phi_c(s) \gamma_{cj} \quad (7)$$

For the contributions from stable two-particle channels, we have

$$\Phi_c(s) = \phi_c(s) \quad (8)$$

with

$$\phi_c(s) = \frac{1}{\pi} \int_{s_{th,c}}^{\infty} ds f_c^*(s') g_c(s'; s) f_c(s') \quad (9)$$

Here  $s_{th,c}$  is the threshold for channel  $c$ , and  $g_c(s)$  is the propagator of the two-particle channel  $c$ . The task now is to choose  $g_c(s'; s)$  such that the unitarity condition Eq.(2) is satisfied and the desired analytic structure of the amplitude can be generated. It can be shown that the  $\phi_c(s)$  of the CMB model is obtained by assuming that

$$g_c(s'; s) = \frac{1}{\pi} \left[ \frac{\rho_c(s')}{s' - s + i\epsilon} - P \frac{\rho_c(s')}{s' - s_0} \right] \quad (10)$$

where the density of states  $\rho_c(s')$  has been defined in Eq.(4), and  $P$  means taking the principle-value part of the propagator. Substituting Eq.(10) into Eq.(9), we then obtain the following dispersion relation for the auxiliary function  $\phi_c$

$$\begin{aligned}\Im m(\phi_c(s)) &= f_c^2(s)\rho_c(s) \\ \Re e(\phi_c(s)) &= \Re e(\phi_c(s_0)) + \frac{s-s_{th,c}}{\pi} \int_{s_{th}}^{\infty} \frac{\Im m\phi(s')}{(s'-s)(s'-s_0)} ds'\end{aligned}\tag{11}$$

We see that Eq.(11) is a subtracted dispersion-relation which has a form similar to what has been established in many studies of  $\pi N$  scattering. In the complex- $s$  plane, one can choose the subtraction point  $s_0$  such that the resulting scattering amplitude has a pole on the left-hand side and a branch cut from  $s_{th,\pi N} = (m_\pi + m_N)^2$  to  $+\infty$ . For each channel, we choose the value at threshold for  $s_0$ , and we set the subtraction constant,  $\Re e(\phi(s_0))$ , such that  $\Re e(\phi_c(s))$  is 0 at threshold. This arbitrary choice has the primary effect of shifting the value of the bare mass squared,  $s_i$ , for each resonance in a partial wave, but does not affect the physical mass of the “dressed” resonance. Here we assume that this dynamical assumption is valid for all stable two-particle channels like  $\eta N$ , and  $K\Lambda$ .

For a quasi two-particle channel  $c$ , the function  $\Phi_c(s)$  in Eq.(7) must account for the mass distribution of one of the two particles which is itself a resonance state. To be specific, let  $m_1$  be the mass of the stable particle in the channel  $c$  and  $m_2$  and  $m_3$  be the masses of the two daughter particles from the decay of the resonant subsystem into a channel  $r$ . Then the form assumed by the CMB model can be more explicitly written as

$$\Phi_c(s) = \int_{(m_2+m_3)^2}^{(\sqrt{s}-m_1)^2} ds_r \sigma(s_r) \phi_c(s_r)\tag{12}$$

where the mass distribution of the quasi particle was taken to be:

$$\sigma(s) = \frac{\gamma_r \Im m(\phi_r(s)) / \pi}{(M_r^2 - s)^2 + \gamma_r^2 \Im m(\phi_r(s))^2}\tag{13}$$

Here  $\phi_r(s)$  is again defined by the subtracted dispersion relation Eq.(11) for the appropriate resonant subsystem. Eq.(13) has the commonly used Breit-Wigner resonance form. The coupling strength  $\gamma_r$  is related to the width  $\Gamma_r$  of the considered resonance state by  $\Gamma_r = \frac{\gamma_r^2 \Im m(\phi(M_r^2))}{M_r}$ . In this work  $r$  is either a  $\pi N$  state or a  $\pi\pi$  state. From the empirical values

of the widths for  $\Delta$  and  $\rho$ , mass distribution functions for the  $\pi\Delta$  and  $\rho N$  channels can be fixed. For the other quasi two-particle channels,  $\sigma N$  and  $\pi N^*(1440)$ , the width  $\Gamma_r$  is fixed at a standard value in the fit [4]. The above formalism for the quasi two-body channels provides a unitarity cut along the real  $s$ -axis from the three-body  $\pi\pi N$  threshold to infinity. Furthermore, it makes the resulting scattering amplitudes satisfy the unitarity condition Eq.(2). This is how the three-body unitarity is implemented in CMB model.

The Dyson equation, Eq.(5), is algebraic and can be solved by inverting a  $N \times N$  matrix. Schematically, we have

$$G_{ij}(s) \equiv [H^{-1}(s)]_{ij} \quad (14)$$

with the matrix element of  $H$  defined by

$$H_{ij}(s) = \frac{s - s_{0,i}}{e_i} \delta_{ij} - \Sigma_{ij}(s) \quad (15)$$

Now all of the ingredients needed for calculating the  $T$ -matrix elements of Eq.(1) are in place. The variable parameters (i.e. couplings  $\gamma_{ic}$  and poles  $s_{0,i}$ ) are then adjusted to fit the VPI-KSU partial wave  $T$ -matrix elements.

### C. Resonance parameter extraction

Following reference [6] a resonance position is identified with a pole of the scattering  $T$  matrix in the complex energy-plane. This can only be done for models that can be evaluated for complex values of  $s$ , i.e. models that have the correct analyticity structure. In the CMB model, the determinant of the  $H$  matrix defined by Eq.(15) equals zero at the pole position,  $s = s_{pole}$ , in the complex  $s$ -plane. Only the poles located close to the real axis are interpreted as resonances. This procedure involves an analytic continuation of  $\phi_c(s)$  into the complex  $s$ -plane for  $\Im m(s) < 0$ . Clearly, the analyticity, defined by the dispersion relation, Eq.(11), plays a “dynamical” role in finding the resonance parameters. This is one of the main differences between our approach and the KSU approach.

To proceed, we need to evaluate Eqs.(11) and (12) for complex  $s$ . Each  $T$ -matrix element has a branch cut beginning at the elastic and each inelastic threshold. The branch cut can have a strong effect on the amplitude, in extreme cases producing a cusp, e.g. in the  $\pi N \rightarrow \pi N$   $S_{11}$  partial wave. Above each threshold, the amplitude is multi-valued. This is traditionally described by a Riemann sheet structure [31]. The amplitude is continuous when analytically continuing to the appropriate new sheet as the value of  $s$  crosses the branch cut, but discontinuous when staying on the same sheet. The function,  $\phi_c(s)$  defined by Eqs.(9) and (10) is the channel propagator for the “first sheet” of the complex  $s$ -plane, labeled  $\phi_{c,I}$ . At  $s \geq s_{th,c}$ , it has a discontinuity in its imaginary part determined by unitarity as  $s$  crosses the real axis.

The resonance pole is on the “second sheet” in which  $\phi_c(s) = \phi_{c,II}(s)$ ; it has the same discontinuity as the first sheet except for the opposite sign,

$$\phi_{c,II}(s + i\epsilon) - \phi_{c,II}(s - i\epsilon) = \phi_{c,I}(s - i\epsilon) - \phi_{c,I}(s + i\epsilon) \quad \text{for } s > s_{th} \quad (16)$$

It is  $\phi_{c,II}(s)$  which is used in the search of the resonance pole positions. Using the same strategy as CMB [6], we search the  $\pi N \rightarrow \pi N$   $T$  matrix for poles on the sheet most directly reached from the physical region. As discussed by Cutkosky and Wang [32] and elsewhere in the literature, each resonance has additional poles on other Riemann sheets associated with each inelastic threshold. However, the pole closest to the physical region is most closely associated with the physical characteristics of the resonance. The formalism presented here can be extended to search for poles on other sheets and try to distinguish between resonance poles and poles that arise from bound states of composite particles.

A resonance pole is found by searching for a zero in the determinant of the  $H$  matrix defined in Eq. (15). Once a pole is found,  $H(s)$  is diagonalized at the pole position  $s_{pole}$ . This is done to eliminate resonance-resonance interference effects when multiple resonances are present in a partial wave. By using the resulting eigenfunctions  $\chi_i$ , the  $T$ -matrix in the vicinity of the pole can be written as [6]

$$T_{ab} = \frac{B_{ab} - \delta_{ab}}{2i} + \sum_{ef} \frac{\sqrt{B_{ae}} \sqrt{\Im m(\phi_e)} \eta_e \eta_f \sqrt{\Im m(\phi_f)} \sqrt{B_{fb}}}{D(s)} \quad (17)$$

The  $\eta_c$  describe the coupling of the resonance to channel  $c$ , as defined in Eq. 19. This form can be shown to be equivalent to the full CMB model. Eq. (17) is a general form for a Breit-Wigner resonance shifted by nonresonant (background) reaction mechanisms. To determine the resonance properties, we look at the  $T$  matrix in the vicinity of the pole with a simplifying assumption. The form of the background part,  $B_{ab}$ , is assumed to be smooth in the immediate vicinity of a pole. This allows us to use the denominator,  $D(s)$ , to define the Breit-Wigner resonance parameters at the pole, ignoring the background. The denominator of the above expression is then matched to a relativistic Breit-Wigner form. The full denominator can be written as

$$D(s) = r - s - v \sum_c y_c \phi_c \quad (18)$$

where

$$y_c = |\eta_c|^2 = \left| \sum_{i=1}^N \gamma_{ic} \chi_i \right|^2. \quad (19)$$

The real constants,  $r$  and  $v$ , are defined by equating  $D(s_{pole}) = 0$ . The resonance mass comes from the real part of the denominator and the width comes from the imaginary part.

The general form of the Breit-Wigner denominator for a multi-channel situation is

$$D_{BW} = (W_{res}^2 - s) - i W_{res} \sum_c \Gamma_{res,c} \quad (20)$$

where  $W_{res}$  is the mass of the resonance and  $\Gamma_{res,c}$  is the decay width of the resonance to asymptotic state  $c$ . Thus, shifts in the resonance mass can be identified with the real parts of the denominator and the imaginary part can be identified with a sum over the partial decay widths of the resonance to various channels,  $c$ . To obtain numerical values, we use a linear approximation for the real part of the summation in Eq. 18.

Using the above definitions, the following qualitative statements about the relationship between the resonance parameters and the model parameters can be made. The resonance

width is approximately equal to twice the imaginary part of the denominator at resonance. Because the self energy term in the denominator has strong energy dependence, the physical pole position is shifted from the bare pole by an amount that depends of the value of the coupling parameter ( $\gamma$ ) and both the value and shape of  $\Re\phi(s)$  in the vicinity of the pole. The mass of the resonance is further shifted from the physical pole because the mass is determined on the real axis of the complex energy plane. Shifts from the real part of the bare pole to the mass can be positive or negative; the size of the shift depends on many factors and can be quite large (more information can be found in section V).

Eq. (17) has an energy dependent pole shift due to  $\Re\phi(s)$ . We wish to remove this energy dependence to make a connection between the full  $T$ -matrix in Eq. (17) and a standard relativistic Breit-Wigner shape. Making the assumption that the “real” part of the term  $\sum_c y_c \phi_c$  is linear close to the resonance pole:

$$v\Re\sum_c y_c \phi_c \approx \alpha + \beta s \quad (21)$$

the  $T$ -matrix can be re-written in the form of a relativistic Breit-Wigner resonance, without an energy dependent pole shift:

$$T_{ab} = \frac{B_{ab} - \delta_{ab}}{2i} + \sum_{ef} \frac{\frac{\sqrt{B_{ae} \Im m \phi_e \eta_e}}{\sqrt{1+\beta}} \frac{\sqrt{B_{fb} \Im m \phi_f \eta_f}}{\sqrt{1+\beta}}}{\left(\frac{r-\alpha}{1+\beta}\right) - s - iv \sum_c y_c \Im m \phi_c / (1+\beta)} \quad (22)$$

In Eq. (22), the quantitative expressions for the resonance parameters can then be identified in terms only of quantities evaluated at the resonance mass :

$$\Re D(M_{res}^2) = 0 \quad \text{Defines Resonance Mass} \rightarrow M_{res}$$

$$\Gamma = \frac{\Im m D(M_{res}^2)}{M_{res} \Re D'(M_{res}^2)} \quad \text{Defines Resonance Width} \quad (23)$$

$$\Gamma_c = \frac{y_c \Im m \phi_c}{\sum_a y_a \Im m \phi_a} \Gamma \quad \text{Defines Branching Fraction into channel c}$$

In the above equations,  $D'(s)$  is the derivative of  $D$  with respect to  $s$ ,  $\Re D'(s) = -(1 + \beta)$ . This term accounts for the fact that there is an energy dependence to  $\Re\phi(s)$ , which shifts the pole position.

This formulation is identical to the generalized Breit-Wigner form that is the basis of most fitting and theoretical models. However, we *only* use this form in the immediate vicinity of the pole to determine the resonance parameters. The *data* are still fit with the full model and the pole position is then determined from that fit. This type of prescription for obtaining the mass, width and partial widths of a resonance is model dependent. It is important to realize that *all* definitions of baryon resonance parameters are model dependent. For a highly elastic and isolated resonance, the model is not very important. However, very few resonances fit this description and we are trying to present a formulation that minimizes the model dependence.

#### D. Relationship to other models

The CMB model has a number of features that are not included in commonly used models. Here, we present a discussion of formulations similar to standard models by making approximations to the full CMB model. These simpler formulas will be used in section IV D to show the corresponding model dependence in the extracted resonance properties.

The full CMB model contains a dispersion relation which guarantees the analyticity. The imaginary part of the channel propagator function (Eq. 11) is the relativistic phase space function and the real part is then calculated from a dispersion integral. Models which are not analytic [4] include only the phase space, so we set  $\Re\phi(s) = 0$  for all  $s$  to simulate them.

The full CMB model uses a Dyson equation to allow for conversion into open intermediate states (resonant or nonresonant) and open asymptotic channels. The bare propagator (Eq. 6) is “dressed” by all the open intermediate and asymptotic states. The  $K$ -matrix formulation [2,23,4,5] uses the bare propagator of the CMB model in place of the dressed propagator as a  $K$ -matrix rather than a  $T$ -matrix and identifies the resonance properties with its parameters. A nonanalytic unitary multichannel  $K$ -matrix using a relativistic Breit-Wigner form [23] can then be constructed for the contribution of resonance  $R$  to the reaction

between initial state  $i$  and final state  $j$ :

$$K_{ij}^R(s) = \frac{\sqrt{\Im m\phi_i(s)} \gamma_{R,i} \gamma_{R,j} \sqrt{\Im m\phi_j(s)}}{s_R - s} \quad (24)$$

where  $\Im m\phi_i(s)$  is the product of the form factor and phase space for channel  $i$  as defined in Eq. (11).  $M_R$  and  $\Gamma_{R,i}$  are the mass and partial width for decay to channel  $i$  of resonance  $R$ ; the total width is  $\Gamma_R$ . These three physical quantities are defined by

$$\begin{aligned} M_R &= \sqrt{s_R} \\ \Gamma_{R,i} &= \frac{\Im m\phi_i(s_R) (\gamma_{R,i})^2}{M_R} \\ \Gamma_R &= \sum_i \Gamma_{R,i} \end{aligned} \quad (25)$$

For the nonrelativistic Breit-Wigner case,

$$K_{ij}^R(s) = \frac{\sqrt{\Im m\phi_i(s)} \gamma_{R,i} \gamma_{R,j} \sqrt{\Im m\phi_j(s)}}{M_R - W} \quad (26)$$

where  $\Gamma_R$  is defined by

$$\Gamma_R = 2 \sum_i \Im m\phi_i(s_R) (\gamma_{R,i})^2 \quad (27)$$

In either case, the corresponding  $T$ -matrix can then be found through the standard definition:

$$T = K * (I - iK)^{-1} \quad (28)$$

Since both  $K$  and  $T$  are matrices, there is no simple closed expression for  $T$  corresponding to Eqs. (24) and (26) except in the single channel case.

Nonresonant  $K$ -matrices must also be defined. To maintain unitarity, the full  $K$ -matrix is obtained by adding all the resonant and nonresonant  $K$ -matrices (e.g. [38]). The corresponding  $T$ -matrix includes effects of resonance interference and coupling to nonresonant processes, but only on-shell.

Various theoretical schemes have been built on the  $K$  matrix method. At low energies, the characteristics of the  $\Delta$  ( $P_{33}(1232)$ ) and the  $S_{11}(1535)$  have been determined with an

effective Lagrangian method [38]. More complete formulations have been developed [33,5]. In these models, the mesons and baryons are each fundamental particles. Although the number of parameters is reduced from what is required for the more empirical models, there are still a number of ambiguities in the construction of the Lagrangian and in the proper development of a multi-resonance, multi-channel model.

### III. DATABASE

We devote a separate section to the database because it plays a critical role in the results we obtain. There are many possible asymptotic states that can couple to each resonance. There are also a number of resonances which couple weakly to the  $\pi N$  channel so that the state is only seen in the inelastic data. Just as it is important to include various inelastic channels with proper threshold effects in the theoretical model, it is also important to include as much of the relevant data as possible with appropriate error bars.

Although it is best to use the original data, various partial wave analyses producing  $T$  matrix representations of the data are available. This kind of analysis can be done with much less model dependence than is found in the analysis used for determination of baryon resonance properties. Nevertheless, these analyses make choices in the data used in the fits and their absolute normalizations since not all data sets are consistent with each other; these choices can add error beyond what was in the original data, thus adding uncertainty to the fit. On the other hand, fitting partial wave amplitudes allows a simpler fitting strategy—separate fits can be made for each partial wave and less computer time is required. This is the same procedure chosen by KSU [4]. We choose to fit the single-energy partial wave amplitudes of the VPI group for elastic scattering [2] and the isobar model fits of KSU-VPI for inelastic pion production [25]. We also make a separate partial wave analysis of the  $\pi N \rightarrow \eta N$  data.

### A. $\pi N$ elastic data

Data in this channel is easiest to measure. Therefore, the data are more complete and of higher quality than in the other channels. In many resonance parameter analyses, these data have a dominant role in the results. This takes advantage of using the best data. However, the inelastic data must be included to find resonances that would not be seen in  $\pi N$  elastic scattering. The Constituent Quark Model [8,18] predicts the existence of a large number of states (roughly a number equal to the number of states seen to date) and finds that many of them couple weakly to the  $\pi N$  channel.

There have been numerous analyses of the elastic data. Since complete experimental results are not yet available, theoretical constraints must be employed to get unambiguous fits. Older analyses of CMB [20] and KH [3] had strong reliance on dispersion relations to generate unique fits. KH80 used fixed- $t$  and fixed- $\theta$  dispersion relations at many angles. The real parts of these results were later compared with partial-wave fixed- $t$  dispersion relation predictions by Koch. [21] Although KH80 results are quite noisy close to threshold in the high  $L$  partial waves, there is good qualitative agreement with the additional constraints. CMB80 uses hyperbolic constraints in the Mandelstam variables.

Although the older works have the best theoretical underpinnings, we use the latest  $\pi N$  elastic partial wave amplitudes of VPI [2]. The VPI analysis uses a significantly larger data set than was available for the earlier CMB80 and KH80 elastic analyses. Most of the new points are at  $W < 1600$  MeV, but there are also many new results at higher energies [2]. Thus, a number of older data points with significantly larger estimated errors could be dropped from the fit, resulting in an improved fit. These more recent results are consistent with fixed- $t$  dispersion relations at  $\theta = 0$  and low  $W$ . Although improvements in the VPI analysis are expected, we use this somewhat debatable [22] approach in this work since this provides a way to include all of the data published since the older work. Desire for an update of the 1980's work has been expressed at conferences for several years, but no such work is in progress.

## B. $\pi N \rightarrow \pi\pi N$ data

For the best available representation of inelastic data, the choices are much more limited than for elastic data. Since there are no model-independent methods for the 3-body final states, isobar models are employed. Since no recent interpretation of the  $\pi N \rightarrow \pi\pi N$  data is presently available, we use the quasi-two-body channel decomposition of Manley, Arndt, Goradia, and Teplitz [25]. That work fit an isobar model to the  $\pi N \rightarrow \pi\pi N$  data, isolating the contributions of  $\pi\Delta$ ,  $\rho N$ ,  $\sigma N$  (with  $\sigma$  representing the  $\pi\pi$  strength in an isoscalar  $s$  wave), and  $\pi N^*(1440)$  channels. Although the  $\sigma N$  channel will absorb some of the nonresonant  $\pi\pi N$  strength, these choices ignore some of the non-resonant  $\pi\pi N$  strength and states such as  $\pi N^*(1520)$  that might be expected to share strength. They used a data sample of about 241,000 events spread over 1320-1910 MeV in W; statistical accuracy is much poorer than for the elastic channel and there is no data at the highest energies where resonances are found. All data published after this analysis were very close to threshold. It will be clear from our analysis that these data need augmentation and that the isobar analysis should be repeated.

As with the choice in elastic data amplitude, this choice is a compromise between including all the existing data in a simple form and using a more proper analysis. An analysis the  $\pi N$  inelastic data without the assumption of the isobar model would be extremely difficult and unjustified with the quality of the present data set.

In the CMB analysis [6,32], the  $\pi N \rightarrow \pi\pi N$  data were weighted by a factor of 1/3 smaller than the results of Manley, *et al.* [25] because they felt the errors were understated. We have a similar attitude and weight the inelastic data by a factor of 1/2. Otherwise, the fits to the higher quality elastic data are degraded.

### C. Description of the $\pi N \rightarrow \eta N$ Analysis

The most significant inelastic channel at low  $W$  is the  $\eta N$  state; data involving this channel is thought to be crucial in analyzing  $S_{11}(1535)$  because the s-wave  $\pi N \rightarrow \eta N$  cross section is large and rapidly changing close to the resonance mass. Unfortunately, the data in this channel is both limited and of uncertain quality. [29] The data set with the most points close to threshold was published by Brown, *et al.* [28]. Clajus and Nefkens [29] argue that these data have unknown errors in the assigned values of  $W$ , making them unusable. As mentioned earlier, Batinic *et al.* [27] put a very small weight on these data points in their partial wave fit to the  $\pi N \rightarrow \eta N$  data. To produce partial wave amplitudes for this reaction, we reproduce the Batinic *et al.* fit to the  $\pi N \rightarrow \eta N$  data, effectively leaving out the controversial Brown *et al.* [28] data set.

Since there is very little data available for the reaction  $\pi N \rightarrow \eta N$ , we use a simplified version of the full CMB model to simultaneously fit the  $\pi N$  elastic  $T$  matrices and the  $\pi N \rightarrow \eta N$  data to provide a parameterization for each of the partial waves with  $L \leq 4$  contributing to the  $\eta$  production cross section. The partial wave analysis followed the procedures used by reference [27], but used the newest VPI  $\pi N$  elastic partial wave amplitudes [2] instead of the older Karlsruhe Helsinki (KH80) amplitudes. The channels used in the analysis are  $\pi N$ ,  $\eta N$ , and a dummy channel consisting of a fictitious meson with mass chosen so that the dummy channel opens at about the energy where  $\pi N$  inelasticity due to channels such as  $\pi\pi N$  start. The mass of that fictitious meson changes from partial wave to partial wave. The values used in the analysis are given in Ref. [27]. The partial waves used are the  $I=1/2$  partial waves through  $G_{17}$ . All partial wave parameters were varied simultaneously. More details on this procedure given in this section can be found in the references [27,30].

For this process, the  $S_{11}(1535)$  resonance makes up most of the total cross section. Therefore, the  $S_{11}$  partial wave is the most accurately extracted. The other partial wave amplitudes are smaller and less accurately determined. The results of this fit are  $T$ -matrices that best model the partial wave data. The best fit is shown as an error band in the figures of the

results section. For the final fits, 40 data points between threshold and 2.3 GeV were used for each partial wave. This insures that these data provide the appropriate contribution to the total chisquare.

#### IV. ILLUSTRATIVE EXAMPLES- $P_{33}$ AND $S_{11}$ PARTIAL WAVES

The purpose of this section is to introduce features of the model through the examination of specific partial waves. The  $P_{33}$  and  $S_{11}$  partial waves are chosen for this purpose. The  $P_{33}(1232)$  or  $\Delta$  is the best example of an isolated and elastic, i.e. simple, resonance; its characteristics are largely well-established. On the other hand, the  $S_{11}$  partial wave has some of the most interesting structure of all the partial waves contributing to  $\pi N$  scattering. Because of this structure, extra care must be taken when extracting resonance parameters for this partial wave. Some of the interesting features exhibited in this partial wave are listed below.

1. There are 2 PDG 4\* resonances ( $S_{11}(1535)$  and  $S_{11}(1650)$ ) which overlap significantly.
2. The  $S_{11}(1535)$  has strong coupling to both the  $\pi N$  and  $\eta N$  channels and is very near the  $\eta N$  threshold ( $\approx 1487$  MeV). This produces a strong cusp in the  $\pi N$  elastic  $S_{11}$   $T$ -matrix element.
3. There are 7 decay channels that have measurable coupling to the  $S_{11}$  states, each of which has different phase space which can cause structure in all of the other channels via unitarity.

All of the above features are adequately handled in the CMB Model.

This section will help in understanding the unitarity, analyticity, and other properties of the model, which are especially important in the  $S_{11}$  partial wave. A discussion of the cusp associated with the  $S_{11}$  partial wave will also be given. Furthermore, this section will present a systematic study of the model dependence of resonance parameters extraction by examining results obtained when leaving out various features of the full CMB model.

### A. Single Channel-Single Resonance Case

The equations from section II give expressions for a reaction  $T$ -matrix element for any number of open scattering channels or asymptotic states ( $\pi N$ ,  $\eta N$ , etc.) and any number of intermediate states ( $S_{11}(1535)$ ,  $P_{33}(1232)$ , etc.). The  $T$ -matrix elements for one asymptotic state and one intermediate state are much simpler. The resulting equations can then be applied with good success to the  $P_{33}$  partial wave near the  $\Delta(1232)$  resonance. Despite the complexity of the CMB formulation, the  $T$ -matrices for an isolated, single channel resonance have a form similar to that found in the Breit-Wigner shapes commonly used.

The one asymptotic state-one intermediate state case requires two parameters (using  $\Delta$  to label the  $P_{33}(1232)$  intermediate state and  $\pi N$  as the asymptotic state), one coupling  $\gamma_{\Delta,\pi N}$  and one *bare* pole energy,  $s_{\Delta}$ . Since there is only one intermediate state the matrix equations are reduced to scalar equations and the math is simple. There is only one channel propagator  $\phi_{\pi N}$  which is determined analytically with a contour integral. (There is a functional form for the channel propagator only in the S-wave case. The results for the  $\pi N$  channel in an S-wave are shown in figure 3.) There is also one self energy term according to Eq. 9.

$$\Sigma_{\Delta,\Delta}(s) = \gamma_{\Delta,\pi N}^2 \phi_{\pi N}(s) \quad (29)$$

Since the function  $\phi$  varies with energy,  $\Sigma$  does also. The  $H$  matrix is then defined by:

$$\begin{aligned} H &= (s_{\Delta} - s) - \Sigma_{\Delta,\Delta} \\ &= (s_{\Delta} - s) - \gamma_{\Delta,\pi N}^2 \phi_{\pi N} \end{aligned} \quad (30)$$

The  $G$  matrix (the dressed propagator) is then calculated from  $H$  as defined by Eqs. (14) and (15) in section II:

$$G = \frac{1}{(s_{\Delta} - s) - \gamma_{\Delta,\pi N}^2 \phi_{\pi N}} \quad (31)$$

$T_{\pi N,\pi N}$  is defined using Eq. (1) and the above equations:

$$T_{\pi N,\pi N} = \frac{\gamma_{\Delta,\pi N}^2 \Im m \phi_{\pi N}}{(s_{\Delta} - s) - \gamma_{\Delta,\pi N}^2 \phi_{\pi N}} \quad (32)$$

The results of a model calculation for the  $T$  matrix is shown in Fig. 4 with a solid dot at the physical resonance mass. The equations produce the characteristic shape of a resonance with a maximum in the imaginary part and a zero in the real part at the resonance mass. A similar signal should be seen for strong resonances, but there will be shifts in the real data when underlying backgrounds of varying smoothness are included.

Eq.32 has the usual form of a relativistic Breit-Wigner resonance as expected, but there are some important new features. The real part of the pole is shifted from the bare pole energy ( $s_\Delta$ ) by  $\gamma^2 \Re\phi(s)$  and the pole gains an imaginary part,  $\gamma^2 \Im m\phi(s)$  due to couplings of the resonance to the asymptotic state as it propagates. In this model, these shifts are energy dependent and come from both unitarity and analyticity requirements. The analyticity condition, Eq. (11) then allows an analytical continuation of the above expressions to the complex  $s$  plane where the *physical* pole position, mass, and width of the resonance must then be determined by a search discussed in section II.

In other contexts, unitarity requirements are satisfied through inclusion of final state interactions. These methods add terms to the denominator similar to what comes from the CMB model. However, these models are not analytic.

Near the resonance peak, Eq. 32 can be expressed in terms of a mass and width identical to a generalized Breit-Wigner shape. Thus, the features of the CMB model can be absorbed into effective constants for the case of an isolated resonance.

## **B. Two Channel- Two Resonance Case**

The equations get rapidly more complicated as the number of resonances and open channels in a partial wave increases. The two channel (or asymptotic states) two resonance (or intermediate states) case is still instructive. The relevant equations are given below for the  $L = 0$  isospin 1/2 ( $S_{11}$ ) partial wave. In reality, this partial wave has two strong channels and two strong resonances. The results shown below use realistic parameters for these states, but are not meant to be an accurate representation of data because non-resonant processes

and other channels are ignored. For clarity, channel labels  $\pi N$  and  $\eta N$  and resonance labels of 1535 (referring to  $S_{11}(1535)$ ) and 1650 (referring to  $S_{11}(1650)$ ) are used. Parameters that must be determined include four coupling strengths ( $\gamma_{1535,\pi N}$ ,  $\gamma_{1535,\eta N}$ ,  $\gamma_{1650,\pi N}$ , and  $\gamma_{1650,\eta N}$ ) and two bare poles ( $S_{1535}$  and  $S_{1650}$ ).

The terms in the  $\Sigma$  self energy matrix are constructed from Eq. (7):

$$\begin{aligned}\Sigma_{1535,1535} &= \gamma_{1535,\pi N}^2 \phi_{\pi N} + \gamma_{1535,\eta N}^2 \phi_{\eta N} \\ \Sigma_{1535,1650} &= \gamma_{1535,\pi N} \gamma_{1650,\pi N} \phi_{\pi N} + \gamma_{1535,\eta N} \gamma_{1650,\eta N} \phi_{\eta N} \\ \Sigma_{1650,1650} &= \gamma_{1650,\pi N}^2 \phi_{\pi N} + \gamma_{1650,\eta N}^2 \phi_{\eta N}\end{aligned}\tag{33}$$

The  $\Sigma$  matrix is symmetric by construction so it takes on the simple form:

$$\Sigma(s) = \begin{pmatrix} \Sigma_{1535,1535} & \Sigma_{1535,1650} \\ \Sigma_{1535,1650} & \Sigma_{1650,1650} \end{pmatrix}\tag{34}$$

Fig. 5 shows the  $\Sigma_{1535,1535}(s)$  function. It is a weighted sum of  $\phi_{\pi N}$  and  $\phi_{\eta N}$ , shown in Fig. 3, and thus carries the threshold behavior of both the  $\eta N$  and  $\pi N$  channels. The other elements have similar qualitative behavior, but varying weights of  $\phi$  because the two resonances couple to the two asymptotic channels with different strength.

The  $H$  matrix becomes:

$$\begin{aligned}H(s) &= (s_i - s) - \Sigma(s) \\ &= \begin{pmatrix} s_{1535} - s - \Sigma_{1535,1535} & -\Sigma_{1535,1650} \\ -\Sigma_{1535,1650} & s_{1650} - s - \Sigma_{1650,1650} \end{pmatrix}\end{aligned}\tag{35}$$

The dressed propagator, the  $G$  matrix, has a simple form since it is a  $2 \times 2$  matrix:

$$\begin{aligned}G &= H^{-1} \\ &= \frac{1}{|H|} \begin{pmatrix} s_{1650} - s - \Sigma_{1650,1650} & \Sigma_{1535,1650} \\ \Sigma_{1535,1650} & s_{1535} - s - \Sigma_{1535,1535} \end{pmatrix}\end{aligned}\tag{36}$$

where  $|H|$  is the determinant of  $H$ :

$$\begin{aligned}|H| &= (s_{1535} - s - \Sigma_{1535,1535})(s_{1650} - s - \Sigma_{1650,1650}) \\ &\quad - \Sigma_{1535,1650}^2\end{aligned}\tag{37}$$

The  $T$  matrix elements are then defined in section II in Eq. (1). Explicitly the  $\pi N$  elastic  $T$ -matrix element is:

$$\begin{aligned}
T_{\pi N, \pi N} = & \frac{\gamma_{\pi N, 1535}^2 \Im m \phi_{\pi N}}{s_{1535} - s - \Sigma_{1535, 1535} - \frac{\Sigma_{1535, 1650}^2}{s_{1650} - s - \Sigma_{1650, 1650}}} + \\
& \frac{\gamma_{\pi N, 1650}^2 \Im m \phi_{\pi N}}{s_{1650} - s - \Sigma_{1650, 1650} - \frac{\Sigma_{1535, 1650}^2}{s_{1535} - s - \Sigma_{1535, 1535}}} + \\
& \frac{2\gamma_{\pi N, 1535} \gamma_{\pi N, 1650} \Sigma_{1535, 1650} \Im m \phi_{\pi N}}{(s_{1535} - s - \Sigma_{1535, 1535})(s_{1650} - s - \Sigma_{1650, 1650}) - \Sigma_{1535, 1650}^2}
\end{aligned} \tag{38}$$

Note that all the functions used in this expression depend on  $s$ . The above expression is the sum of two resonances with an interference term. (If there is only one resonance, this formula simplifies to the same as Eq. (32).) The terms that look like single resonances are more complicated than in the previous example. The self energy terms have the necessary analytic cuts from the  $\eta N$  as well as the  $\pi N$  channels and also make the amplitude unitary. There are analogous  $T$ -matrix elements for the processes:  $\pi N \rightarrow \eta N$  and  $\eta N \rightarrow \eta N$ .

In this case, two poles must be found in the complex energy plane. Since the two resonances have significant interference, the non-diagonal elements of the  $G$  matrix are large. This means the second resonance has a contribution to the propagator of the first resonance at the pole of the first resonance. Referring to Eq. (38), there are shifts to the mass and width of each resonance due to the presence of the other in addition to those due to the asymptotic channel couplings which were not seen in the one channel-one resonance case. Here, the  $H$  matrix (the inverse of  $G$  or the “denominator” matrix) must then be diagonalized at each pole to isolate the contributions from each individual resonance.

The  $\pi N$  elastic and  $\pi N \rightarrow \eta N$   $T$  matrices in this partial wave corresponding to the above equation for representative parameters (see Table I and II for a complete listing of the relevant values) are shown in Fig. 6. The eta threshold has a significant effect on the observables. Therefore, the  $\pi N$  elastic  $T$ -matrix element peaks at the  $\eta N$  threshold rather than at the peak of the  $S_{11}(1535)$  resonance. The physical masses are shown as solid dots which are near the peak of the cross section and the imaginary part of  $T$  for the higher state, but above those positions for the lower state. For all channels, the peak of the  $T$ -matrix is

shifted by a few dozen MeV from the bare mass by the self energy terms. (The  $S_{11}(1535)$  resonance shape is also modified by the presence of a strong inelastic threshold.) There is also significant interference between the two resonances. Both cross section bumps are unusually narrow compared to the physical widths because of interference effects. We find that the  $S_{11}(1535)$  properties are significantly altered by the interference with  $S_{11}(1650)$ , similar to the findings of Sauermann, Friman, and Nörenberg [33] in a  $K$ -matrix photoproduction calculation.

### C. Cusp structure in the $S_{11}$ partial wave

There are two main causes of the strong cusp structure observed in  $\pi N$  elastic scattering differential cross section, as well as the  $S_{11}$  partial wave amplitudes. The first is that the  $S_{11}(1535)$  resonance couples strongly to both the  $\pi N$  and  $\eta N$  channels and the  $\eta N$  channel threshold ( $\approx 1487$  MeV) is just below the 1535 pole. The second is that the orbital angular momentum is zero ( $\pi N$  S-wave); thus, the cross section in this partial wave increases linearly with momentum. Therefore, through analyticity and unitarity, a cusp structure appears in the  $\pi N$  elastic channel.

Figure 5 shows the self energy term labeled  $\Sigma_{1535,1535}$  for the 2 channel 2 resonance model of Sec. IV B. This self energy has the appropriate analytic phase space factors and therefore shows a cusp. Since  $\Sigma$  enters directly into the  $T$ -matrix elements, the cusp shows up there as well. Figure 8 shows the  $T$ -matrix elements for elastic scattering and  $\rho$  production. Although the cusp structure is apparent in the  $T$  matrices for all channels other than that of eta production, it is most evident in the  $\pi N$  elastic channel because most of the decay width of the  $S_{11}(1535)$  is split roughly equally between the  $\pi N$  and  $\eta N$  channels. All other inelastic channel openings have the potential of creating a cusp, but this is by far the strongest case. At present, the  $\pi N$  data is not of high enough quality to see any other cusp structures.

#### D. Model Dependence in Analysis of the $S_{11}$ partial wave

The variation between this and other models can best be seen in an analysis of the data in the  $\pi N S_{11}$  channel, as discussed in previous sections. Because of the peculiarities of this channel, data for both  $\pi N \rightarrow \pi N$  and  $\pi N \rightarrow \eta N$  reactions would be required for a high quality determination of the  $S_{11}(1535)$  parameters and data for  $\pi N \rightarrow \pi\pi N$  would be required for a good determination of properties for the higher energy states. Presently, the inelastic data is of much less quality than for the elastic channel.

To test model dependence in the resonance parameters, we have analyzed all available and subsets of the data for the  $S_{11}$  channel with the full CMB model and various approximations that simulate the models employed by various other groups. Although the final fits were of similar quality for all cases, there can be large differences in the extracted resonance parameters.

In Tables IV and V, masses, widths and branching fractions are given for the two of the three  $S_{11}$  resonances used in this analysis for a number of different model types using various data sets to constrain the fits. The four columns on the left of the table describe features of the model used and what data was used in the fit. The five columns on the right give the results of the fit for the resonance parameters- mass, width, and branching fractions.

The *Unitarity* column labels how unitarity was imposed in the fits. *K-matrix* means that unitarity was imposed by commonly used *K*-matrix methods of Moorhouse, Rosenfeld, and Oberlack [23]. For the results shown in the tables, we recreate the *K*-matrix fit of Ref. [23] with the appropriate phase space factors ( $\phi(s)$ ) from our model as discussed in Sec. II D. *Dyson equation* means that unitarity was imposed using the Dyson-equation approach of the CMB model. Channels can interact any number of times in various forms before finally decaying because the Dyson equation is iterative.

The column labeled *Disp Rel* refers to whether or not the dispersion relation was used to make the phase space factors in the self-energy terms analytic functions or not. If the dispersion relation is evaluated, the phase space factors and hence the self-energies are

analytic functions of the square of the CM energy,  $s$ ; otherwise they are not. When using the Dyson equation and not evaluating the dispersion relation (in the fits, we set  $\Re\phi = 0.0$ ), all intermediate interactions in the scattering process occur on-shell. Note that this does not affect unitarity. If unitarity is achieved through  $K$ -matrix methods, the mass and widths are direct parameters in the fit.

The column *Res Type* describes the form of resonance used. *NRBW* refers to a non-relativistic Breit-Wigner shape and *RBW* means a relativistic Breit-Wigner shape was used. For the NRBW case, a resonance has a  $\frac{\gamma^2}{w_0 - w - i\gamma^2}$  form and the  $\gamma$  couplings have units of  $\sqrt{\text{energy}}$ . For the RBW case, a resonance has a  $\frac{\gamma^2}{s_0 - s - i\gamma^2}$  form; the  $\gamma$  couplings have units of energy.

Finally, the column labeled *Channels in fit* describes the types of data used in the fit. For the  $\pi N$  case, only the VPI  $\pi N$  elastic  $S_{11}$   $T$ -matrix elements were used in the fit. For the  $\pi N$ ,  $\eta N$  cases both the VPI elastic data as well as constraints from a partial wave analysis of  $\pi N \rightarrow \eta N$  done by this group were used. For cases labeled *All*,  $\pi N \rightarrow \{\pi N, \eta N, \pi\pi N\}$  are all included in the fit. The  $\pi\pi N$  channel is composed of quasi two body channels  $(\rho_1 N)_S$ ,  $(\rho_3 N)_D$ ,  $(\pi\Delta)_D$ ,  $\sigma N$ , and  $\pi N^*(1440)$ . Partial wave quasi-two-body  $T$ -matrix elements of Manley *et al.* [25] are used for these channels.

The last row in each table contains results for our full model. All channels are used in the fit, unitarity comes from use of the Dyson equation, analytic phase space factors are used, and the bare resonance has a *RBW* dependence.

Significant model dependence is seen along with sensitivity to the data used. The lower state ( $S_{11}(1535)$ ) has significant model dependence as noted above while  $S_{11}(1650)$  tends to have poorer quality data, i.e. missing data or data with error bars that are too small. We do not show any results for the third resonance ( $S_{11}(2090)$ ) because the data quality dominates the fitting, causing wide variation in fit results, e.g. masses vary between 1509 and 2028 MeV. The data quality for this partial wave is discussed in detail in section VC.

We note that without the dispersion relation, the  $T$  matrices for the  $K$ -matrix model and the model using the Dyson equation for the resonance propagator are equivalent. Therefore,

only the  $K$ -matrix results without the dispersion relation are given in the table. In general, the choice of relativistic vs. nonrelativistic shape for the bare Breit-Wigner resonance does not have a strong influence for an isolated resonance such as the 1535 MeV state. However, the 1650 MeV state has a weaker signal (in part because of poorer data quality) and the two shapes can produce larger differences. Even there, the agreement in the case where all data is used (line 3 for NRBW vs. line 6 for RBW) is very good.

More important differences are found when comparing  $K$ -matrix vs. Dyson equation results with the dispersion relation included (e.g. line 6 vs. line 9). The former is close to the model employed by Manley and Saleski [4]. These two models have differences of about 10% in the total width and up to 50% in the branching fractions.

The most important deviation from the full result comes from the use of a truncated data set. For the 1535 MeV state, ignoring the interference with the  $\eta N$  final state causes the model to fit the Breit-Wigner shape to the cusp at the  $\eta N$  threshold. The VPI work [2] has a very small width for the 1535 MeV state; although the  $\eta N$  channel is mocked up, none of the actual data is used. For even the full model, leaving out the  $\pi\pi N$  final state data (such as was done by Batinic *et al.* [27]) produces 20% deviations in the branching fractions. We reproduce the updated results of the Batinic *et al.* paper [27].

Both the mass and the width of the  $S_{11}(1535)$  tend to increase as more data channels are added into the fit. It is interesting to note that the small widths (i.e.  $< 100$  MeV) are in situations where only the  $\pi N$  elastic data is used in the fit. Also, the branching fraction of  $\eta N$  tends to be smaller than that of  $\pi N$  unless the analyticity is taken into account in the phase space factor. In other words, when the cusp is handled appropriately, the  $\eta N$  channel becomes the dominant decay mode. The Manley-Saleski [4] analysis, which does not address the analyticity issue, is unable to match the cusp well and concludes that  $\pi N$  is the dominant decay mode.

The  $S_{11}(1650)$  and the third  $S_{11}$  resonance have more random shifts in their resonance parameters. At energies in the region of the excitation of the third  $S_{11}$  state, only elastic and  $\eta$  production data exist and the signal is not strong. Therefore, the fit parameters for

the third  $S_{11}$  state are largely determined by fitting non-statistical fluctuations of the data. The fitted masses vary widely from case to case and we feel the results with the different models do not give information about features of the models.

### **E. Elastic Data Dependence**

A major question is the balance between model dependence and data dependence. The previous section showed the model dependence using various subsets of the data used in this analysis. In this section, we present results for fits of the  $S_{11}$  channel using two different sets of elastic partial wave amplitudes. In Table VI, we compare our standard results with the results of a fit using the combination of CMB80 and KH80 data sets. This fit uses the same elastic data as Manley and Saleski [4] except for the additional  $\pi N \rightarrow \eta N$  data. The differences seen in the table are somewhat similar (in total width) to but somewhat smaller (in branching fraction) than those presented in the previous section, verifying that the major difference between the present work and Manley and Saleski is likely due to model dependence. The changes in the results are larger for the second state than for the lowest state, but the differences are significant for both states. The differences are much larger for the third  $S_{11}$ , but are not shown because of the weak evidence for this state.

The balance between the branching fraction into  $\pi N$  and  $\eta N$  for the lower state are very similar in the two cases, but the total width found using the older data is 22% larger. This gives more evidence for the findings of the previous section that differences in branching fractions are a primary result of the difference between this model and that used by Manley and Saleski.

### **F. The nonresonant amplitude**

A major problem in any extraction of resonance parameters is in the careful separation of resonant and nonresonant mechanisms. Ideally, an independent calculation would be used for the nonresonant diagrams. Here, we choose a more objective strategy and use a smooth

background that can then be “dressed” to contain the correct threshold behavior. To do this, we add two subthreshold resonances (one repulsive and one attractive) and one very high energy resonance in each partial wave as ‘bare’ propagators. These propagators are then dressed identically to the true resonances. More details are given in section II B.

The separation into resonant and nonresonant components is shown in Fig. 8 for various reactions in the  $S_{11}$  partial wave. We show the magnitude of the  $T$ -matrix for four different final states calculated with final fit parameters. The three lines shown correspond to including only nonresonant couplings, only resonant couplings, and all couplings. Since the nonresonant and resonant processes are intermixed in the Dyson equation, there is no way to sum them to get the full result.

While some reactions are dominated by resonant processes (e.g. elastic scattering), others are dominated by the nonresonant processes (e.g.  $\pi N \rightarrow \rho_1 N$ ). The resonance excitation must be sampled through a variety of channels to provide the full picture. At very high energies ( $W \sim 1.9$  GeV), the lack of data allows the nonresonant processes to dominate. Resonance extraction at these high energies is very unclear with the data presently available.

## V. RESULTS AND DISCUSSION

We have applied the CMB model to the database presented in section III-  $\pi N$  single-energy elastic  $T$  matrices of VPI [2], the inelastic  $T$  matrices of Manley, Arndt, Goradia, and Teplitz [25], and our own partial wave analysis of the  $\pi N \rightarrow \eta N$  data. The  $\pi N \rightarrow \pi\pi N$  raw data was not available in time for the present analysis. A reanalysis of the  $\pi N \rightarrow \pi\pi N$  data is in progress [34] by our group; a more complete analysis can be presented when that work is finished.

The analysis presented here contains features of CMB [6] and KSU [4] since we use the formalism of the former and a data set similar to that used by the latter. However, the present analysis goes beyond any previously published. We present general results and a detailed discussion of the  $D_{15}$ ,  $D_{13}$ , and  $S_{11}$  partial waves.  $D_{15}$  is an excellent example of an

isolated resonance, but has strong inelastic couplings. The  $D_{13}$  and  $S_{11}$  partial waves each have a strong state (well understood for the former and poorly understood for the latter) along with less well understood states; the interpretation of most of these states are sensitive to the features of the present model.

We will compare our results to previous work with an emphasis on works that treat many channels. We also compare to the composite results of PDG [1].

### A. Details of Fitting

Although the  $\pi N \rightarrow \pi\pi N$  data set used here is identical to that used by KSU, they do not include the  $\pi N \rightarrow \eta N$  data and use older elastic analyses. KSU includes an  $\eta N$  channel in the  $S_{11}$  partial wave fit, using the requirements of unitarity to fix its coupling strength to the resonances. For the elastic channel, they use CMB and KH80 elastic amplitudes simultaneously.

For the inelastic channels involving two pions, we define channels identical to those chosen in Ref. [4]. They are listed in Table III. Each channel has a specific orbital and spin angular momentum; the nomenclature used is given in the table. These  $\pi N \rightarrow \pi\pi N$  channels are almost identical to those chosen in Ref. [25]. The only difference is in the choice of the mass and width of the fictitious isoscalar-spin 0 meson, taken as 1 GeV for each parameter in Ref. [25]; like Ref. [4], we choose a mass and width of 800 MeV. We agree with their conclusion that the results are not sensitive to this choice.

The number of states sought in each partial wave was the same as used by KSU [4]. We also included the same number of open channels in each partial as KSU because of the choices in the amplitudes fitted in Ref. [25]. If no amplitudes are provided by Ref. [25] for a partial wave, e.g. for  $F_{17}$ , an appropriate dummy channel is used to absorb the flux. Table VIII labels rows of this type as ‘Flux’.

The number of parameters depends on the number of resonances to be fit and the number of open channels included in the fit. For example, the  $S_{11}$  partial wave has three resonances

and we fit values for each bare pole and its couplings to as many as 8 channels. There are also two subthreshold and one high energy “states” used to simulate background. The masses of these states are constrained to be far away from any of the actual resonances. Three parameters, a pole and coupling strengths to  $\pi N$  and  $\eta N$  are fit for each subthreshold background pole. The high energy state is allowed to couple to all open channels. Thus, there are 38 parameters fit in this partial wave. For the  $D_{15}$  partial wave, only one resonance (with coupling to four channels) and three background poles were fit, a total of 15 real parameters.

In the elastic channel, the data quality is reasonable at values of  $W$  from threshold to about 2.0 GeV. At values of  $W$  larger than roughly 1.8 GeV, no inelastic data is available for the  $\pi\pi N$  final state. The inelastic data has significant fluctuations. If the data are to be represented by a smooth function (assumed in all analyses), the error bars are underrepresented. In fact, the Manley *et al.* paper [25] states that only diagonal errors were included in their output. Correlations should be significant in the analysis and can only add to the uncertainties. Although the elastic data were able to be fit well, the inelastic data were not. Since the elastic data is of much higher quality than the inelastic data, the inelastic error bars were weighted by a factor of 2 lower than the elastic error bars in order to ensure a reasonable fit to the elastic data. (The original Cutkosky, et al. paper [6,32] used a factor of 3 to weight the inelastic data.) For elastic data, values of  $\chi^2/datapoint$  were 1.7 and 1.6 for the  $S_{11}$  and  $D_{15}$  waves, respectively. For the inelastic amplitudes,  $\chi^2/datapoint$  values were 9.2 and 22.2. The  $\chi^2$  values are given for the partial wave amplitude values without the extra weighting factor. (We don’t quote  $\chi^2$  per degree of freedom because the parameters are shared between the elastic and inelastic fits.) Although we get qualitatively better fits to the elastic data than Manley and Saleski [4] in most cases, similar quality fits are found for the inelastic amplitudes. (No values of  $\chi^2$  are given by KSU.) However, the shapes of our inelastic  $T$  matrices are qualitatively different in many cases. Specific partial waves will be discussed in section VC.

For a complicated multi-parameter fit, errors are difficult to determine because correlations can be significant. The partial wave data we use as input quotes only diagonal errors.

We include error estimates in all extracted quantities due to propagation of errors quoted in the partial wave data. In addition, we add contributions determined from additional fits where the background parameterization is varied.

To allow a full error analysis, separate fits were made to data over a limited energy range to isolate single resonances. A  $2 \times 2$   $K$  matrix was used to model 2 channels at a time and a number of fits were made for each resonance to determine errors on each of the extracted quantities. In one fit, the errors on the resonance mass and width and the error on the largest branching ratio were determined. With  $\pi N$  as one channel and the channel with the largest remaining branching fraction (often  $\pi\Delta$ ) for the resonance under consideration as the second channel, the resonance mass, width, and branching fraction together with a simple parameterization of the nonresonant amplitude were fit to the data. Errors for the branching fraction to the channels with less coupling strength were determined in fits where the mass and width of the resonance were fixed at the final fit value of this work and only the branching fraction and background were fit. For the  $K$  matrix in these cases, the channel for which the branching fraction was being determined was one  $K$ -matrix channel and the  $\pi N$  channel or the channel with the largest branching fraction was chosen as the second  $K$ -matrix channel. In all cases, two fits were done with different simple assumptions for the background dependence, either flat vs. linear or linear vs. quadratic. The first type was most often used. Two components to the error for each parameter under study were determined from each pair of fits, a *relative error* for each fit parameter from the fit with the largest  $\chi^2$  and the absolute difference between the two determinations of the fit parameter. The first component is representative of the statistical error in the data points; the second error is due to systematic effects between the different background parameterizations. When two reasonable fits were obtained, the components were added in quadrature. For prominent states, the fits were easily made. However, most states required many trials to find fits of the appropriate quality. Background shapes, channel choices,  $W$  ranges, and weighting of the inelastic channel in the  $\chi^2$  determination were all varied until two good fits were obtained. All error bars quoted in the tables discussed below were determined from these fits.

## B. General Results

A list of resonances found in this analysis is given in Tables VII and VIII and compared to the results of KSU [4], those of CMB [6] and the latest recommended values given by PDG [1]. For various states, many other results exist. We make direct comparisons only with the previous results that use multi-channel models and provide error bars for their determinations. We show masses and widths in Table VII and branching fractions to various inelastic channels in Table VIII. These are the results of the analysis discussed in sect. II C. Poles corresponding to most of the states found by KSU are found in this analysis, although the properties can be different; states for which there is no evidence in the present analysis are  $P_{13}(1900)$ ,  $F_{15}(2000)$ , and  $D_{33}(1940)$ , all of which are  $1^*$  states according to PDG [1]. Although we obtain fit results for many weak states, a detailed study of the validity of the fit for weak states was not attempted. Discussion in this section will be limited to PDG  $3^*$  and  $4^*$  resonances. In Table IX, we show the results for pole positions of this analysis. The pole positions have less model dependence than the parameters in Tables VII and VIII.

The analysis presented here is not identical to any previous analysis. The data base used is similar to KSU, but the formalism has significant differences. The formalism is identical to CMB, but the data base used is quite different. CMB used the best representation of data at the time- their own elastic amplitude analysis [20] and the inelastic quasi-two-body amplitudes of the SLAC-Berkeley [35] and Imperial College [36]. Batinic *et al.* [27] use a truncated version of the formalism used here and still another data set.

Strong isolated resonances that have a strong elastic coupling are fit well with all models and results for the resonance parameters, such as the  $D_{15}(1675)$  and  $F_{15}(1680)$  masses and widths, tend to have close agreement between previous results and the new results. PDG gives a range of 15 MeV for both masses and a range of 40 and 20 MeV for the  $D_{15}$  and  $F_{15}$  full widths and our values are within these intervals. For the elastic branching fraction, PDG suggests a range of 10%; our results are inside the range for  $F_{15}$  and just outside it for  $D_{15}$ .

The benefit of the multichannel analysis is readily apparent for states with a very small elastic branching fraction. For example,  $D_{13}(1700)$  and  $P_{11}(1710)$  (both PDG  $3^*$  resonances) are not seen in the VPI elastic analysis [2] because there are no strong signs of the resonance in the elastic  $T$  matrix. However, there is a strong resonance signal in the  $\pi N \rightarrow \pi \Delta$   $T$  matrix in each case.

For the cases where KSU differs significantly from the consensus of previous results, the  $S_{31}(1620)$  mass and the  $S_{11}(1650)$  elasticity, the new results tend to agree with the older values. To test for the dependence on the elastic data used in the fit, we re-did fits with the same elastic data used by KSU and found results qualitatively similar to our final analysis.

An unusual feature of the CMB analysis is the large value for the  $S_{11}(1535)$  width, about 40% larger than any other analysis. This analysis obtains a width in closer agreement with KSU and KH than CMB. We have been unable to reproduce the large width. We note that CMB based their fit on a subsidiary analysis of Bhandari and Chao [37] with a compatible model. Although the  $\pi N \rightarrow \eta N$  data has changed little since then, the elastic data we use is a global fit to all data rather than the single data set they used. The VPI SM95 single energy solution is systematically larger and somewhat flatter than the data used in that 1977 work. The most confusing aspect is that Bhandari and Chao quote a full width of  $139 \pm 33$  MeV, much more compatible with the present results than with the full CMB results.

There has been significant interest and controversy in the properties of states in the  $P_{11}$  partial wave. In large part this is because the data in this partial wave has always been poor. In the present fit,  $\chi^2/datapoint$  for this partial wave is 3.8 for the elastic channel and ranges from 8.5 to 17.6 for the inelastic channels. With the low quality of the existing inelastic data, no effort was made to determine the correct number of  $P_{11}$  states. We find three  $P_{11}$  states with properties somewhat different than those previously obtained, although all of our values are within the suggested ranges of PDG. In our results,  $P_{11}(1440)$  has a mass that just overlaps the PDG window and one of the largest widths obtained. In our fit, this state has a significant contribution from nonresonant interactions; that together with the low quality of the present data produces a large estimated error for the values given. KSU

results for this state show a somewhat smaller width and a much smaller error bar. We can only comment that the KSU model handles background quite differently than the present model and they used older  $\pi N$  elastic data. For the  $P_{11}(1710)$ , we find mass and width values well within the large PDG ranges; however, KSU has a very large width with a large estimated error. Since this state sits on the tail of the  $P_{11}(1440)$  and doesn't have a strong signal in any channel, it is clear that the properties of the 2 lowest  $P_{11}$  states are closely coupled and multichannel analyses are very appropriate. A later analysis of Cutkosky and Wang [32] of this partial wave using the CMB model compared results obtained with the VPI (SM89) and CMB80 partial wave analyses. They find qualitatively similar results (large width for the Roper and small width for the 1700 MeV state) to those obtained here. Evidence for the highest energy  $P_{11}$  state in the present data is very poor because only elastic data exists in the appropriate energy range.

Other unusual cases found in this new analysis include the  $P_{31}(1910)$  and  $S_{31}(1900)$  states. The  $P_{31}(1910)$  is found at significantly higher mass and has significantly larger width than previous determinations. Since this state is at high mass, the inelastic data is very important in determining its properties. However, there is almost no existing inelastic data in this partial wave other than a few points in the  $\pi N \rightarrow \pi N^*(1440)$  reaction. PDG has given this state a 4\* rating, but with the present data this rating should be downgraded. Although VPI doesn't find the  $S_{31}(1900)$  state, it is very prominent in KSU and PDG. We find the mass at 1802 MeV and a width of 48 MeV (with a large estimated error) while KSU finds 1950 MeV and 263 MeV. This significant difference is largely due to the elastic data sets used. There is a strong bump at about 1900 MeV in the elastic  $T$  matrices used by KSU which has vanished in the VPI partial wave amplitudes.

For the branching fractions presented in Table VIII, the only recent result is KSU, which is presumably weighted heavily in the PDG listings (also shown in the table). We divide the  $\rho N$  and  $\pi\Delta$  channels into the appropriate spin channels since the component angular momenta can sometimes have more than one value. For  $D_{13}$ , the  $\rho N$  spin can be 1/2 with orbital angular momentum 2 or 3/2 with orbital angular momentum 0 or 2. Since only the

spin 3/2 orbital angular momentum 0 case was found to be important in the  $\pi N \rightarrow \pi\pi N$  isobar analysis [25], this is the only  $\rho N$  channel we include for this partial wave. The  $\pi\Delta$  channel can couple with orbital angular momentum of 0 or 2 in this partial wave and both possibilities are included in the fits.

As with KSU, uncertain fits due to underestimated error bars and/or missing data make interpretation difficult in some cases. We quote values for this analysis and give estimated errors for each quantity.

Since we use the same inelastic  $T$  matrices as KSU for input to the fit, the results should be qualitatively similar. Based on our study in section IV D, we feel there is roughly 20% difference between the KSU and Pitt-ANL results due to model dependence in the most sensitive quantities. The poor fits make this true less often than might be expected. For  $F_{15}(1680)$ , the elastic branching fraction is  $\sim 70\%$  in both analyses and the largest inelastic channels are  $\pi\Delta$  P-wave and  $(\pi\pi)_s N$  in both; agreement is within errors for the largest values. For  $D_{33}(1700)$ , the elastic branching fraction is small and the inelastic strength is concentrated in the  $\pi\Delta$  s-wave, so we are in close agreement with KSU. However,  $S_{31}(1620)$  is a strong state where agreement is not good. There are 2 strong inelastic channels,  $\rho_1 N$  and  $\pi\Delta$  D-wave. Although there is agreement in the strength of  $\rho_1 N$ , the elastic strength is much smaller for KSU and the  $\pi\Delta$  branching fraction is of course larger. The full widths seen are only 15% different and the estimated errors overlap. The  $\chi^2$  per data point for the  $S_{31}$  partial wave in the elastic channel is 2.1 and ranges from 4.3 to 17.2 for the inelastic channels.

The calculation of Capstick and Roberts uses a relativized quark model to calculate resonance masses and a  ${}^3P_0$  model for creation of  $q\bar{q}$  pairs [18]. They fit the two quark level coupling parameters to the  $\pi N$  decay amplitudes of the non-strange resonances rated by PDG as 2\* or better and then predict the remaining decay amplitudes for various meson+baryon final states (including many final states for which there are no data). Although their primary purpose was to look for signatures of “missing” quark model resonances, we note that the qualitative agreement with our analysis is satisfactory. There are notable

successes such as  $D_{13}(1520)$  where quantitative agreement comes with all significant decay channels and notable failures such as  $S_{11}(1535)$  where both  $\pi N$  and  $\eta N$  decay widths (and the full width) are overestimated by a factor of 4.

### C. Detailed Discussion - $D_{15}$ , $D_{13}$ , and $S_{11}$ Partial Waves

Presented in this section are detailed results for three representative partial waves. It includes figures of all the channel  $T$  matrices and a discussion of the results. These partial waves have reasonable quality data and contain both prominent and less prominent states. Numerical data can be found in Tables IV, V, VIII, and VII. The  $T$  matrices are found in figures 9 for the  $D_{15}$  partial wave, 10 for  $D_{13}$ , and 11 for  $S_{11}$ . In each we show the relevant phase shift amplitudes [2,25] along with the fit of Manley and Saleski [4] (dashed lines) and our final fit (solid line). Only data up to  $W=2.15$  GeV were used in the fits because the data at higher values of  $W$  are of diminished quality. Since all the data in each partial wave were simultaneously fit with the requirements of unitarity, not all channel data shown in the figures is fit equally well. In general, the fits to the elastic data are good ( $\chi^2/datapoint \sim 2$ ) and the fits to the inelastic data are poor ( $\chi^2/datapoint > 10$ ) for both the KSU fits and the present results, as discussed above.

The  $D_{15}$  partial wave contains a strong (PDG [1] 4\*), isolated resonance for which the results of the one resonance example (see section IV A) apply fairly well. In this case, both the elastic and  $\pi N \rightarrow \pi\Delta(Dwave)$  inelastic channels are prominent in the  $D_{15}$  partial wave. Since neither threshold is nearby and there is no interfering resonance, the  $T$  matrix in each of these channels has the characteristic shape of an isolated resonance with a peak in the elastic and inelastic cross section near the resonance mass. The non-resonant amplitude is a smooth function. The KSU and present fits are similar in the ability to match features in the data in the two strong channels near the cross section peak at  $W \simeq 1680$  MeV. The two analyses differ in their description of the high energy data ( $W \geq 1.8$  GeV), but the data are very sparse there. Neither model fits the smaller  $\rho$  production channels well. The  $\rho_3 N$

channel shows that the model expectations (based on the requirements of unitarity and the data in the other channels) don't match the data in this channel and a poor fit results.

Essentially all analyses for the  $D_{15}(1680)$  resonance give similar values for the mass, full width, and elastic fraction (see Table VII). Even though VPI [2] accounts for the inelasticity by using a dummy channel, the fit parameters for this state are similar to those obtained in the present fit. PDG [1] gives quite small error bars for the mass and width of this state, reflecting the unanimity of the fitting results for this state. It is encouraging that the complicated features of the present model are not important for the simple case presented in this partial wave.

The  $D_{13}$  partial wave contains a  $4^*$  state at 1520 MeV (PDG standard value, the actual mass is slightly different), a  $3^*$  state at 1700 MeV, and a  $2^*$  state at 2080 MeV. Since the lowest two resonances have significant overlap in energy, the features of the CMB model are important for this partial wave. The lowest state is highly elastic, but also shows up prominently in  $(\rho_3 N)_S$  and  $(\pi\Delta)_S$  final states. Note that the peak in the imaginary  $T$  matrix is inverted. As already mentioned, the second state is barely seen in the elastic channel, thus is not found in the VPI [2] analysis. Both KSU and the present analysis find most of the decay strength in the  $\pi\pi N$  final states with less than 10% of the decay strength to the elastic channel. KSU differs with this model in the distribution of the inelastic strength. While KSU finds most of the strength in  $\rho N$ , this model finds it in  $\pi\Delta$ . The KSU model fits available inelastic data better. Feuster and Mosel [5] find a systematically lower width than other models for the lowest state, but their width for the 2nd state is unusually large. Evidence for the third state is very weak in this analysis; there is only elastic data at  $W \geq 1.9$  GeV and there is very little evidence of structure. It is best fit with a very large width.

The 3 resonances have varying strength in the different channels. As a result, the fitted curve also changes significantly from channel to channel. In the  $\pi\Delta$  channels, the shapes are complicated because the 1700 MeV state is important. The imaginary part of the  $T$  matrix has a dip at the 1520 MeV state and a peak at the 1700 state. Nevertheless, this model and the KSU model fit the features well and the fitted parameters for the higher energy state

agree within stated errors.

The  $S_{11}$  partial wave was already discussed in section IV with regard to the significant model dependence seen. As a result of this model dependence, the  $S_{11}(1535)$  full width has been quoted as 66-250 MeV based on different analyses of similar data (almost all fits are based prominently on the elastic  $\pi N$  channel). The relatively small width of the  $S_{11}(1535)$  in this analysis ( $112 \pm 30$  MeV) is determined in large part by a significant overlap of the  $S_{11}(1535)$  with the  $S_{11}(1650)$ . This overlap causes a large interference effect. Although a similar effect was seen in one description of the  $\gamma p \rightarrow \eta p$  data that uses a formalism similar to the Pitt-ANL model [33], many models based on a  $T$ -matrix formalism (e.g. [38–40]) have a formalism where it is difficult to account for more than one resonance in a partial wave.

The multichannel  $K$ -matrix analysis of Feuster and Mosel [5] gets values of the full width in the range of 151-198 MeV for different form factors. However, their model doesn't handle the  $\eta N$  cusp as well because it lacks the analytic phase space, doesn't model the  $\pi\pi N$  inelasticity well because a zero width particle is used, and doesn't include off-shell intermediate state scattering effects because of the  $K$ -matrix approximation.

Although 8 channels are included in the fit, many of them turn out to have small coupling to  $S_{11}(1535)$  (in agreement with PDG [1]). The two major channel couplings for  $S_{11}(1535)$  are  $\pi N$  and  $\eta N$ . Therefore, another determining factor in the full width is the total cross section for the  $\pi^- p \rightarrow \eta n$  in Fig. 12 and the corresponding  $T$  matrix in Fig. 11b. The cross section of Fig. 12 is made up of  $\pi N \rightarrow \eta N$   $T$ -matrix amplitudes for  $S_{11}$  through  $G_{17}$ , however its main component is  $S_{11}$ . Although the shape of the cusp (see Fig. 7) does carry information about the  $\eta N$  channel, the overall data quality isn't satisfactory. We await higher quality data for a more conclusive determination of this amplitude.

The branching fraction of the  $S_{11}(1535)$  to the  $\pi N$  channel is at the low end of the PDG range. A surprising feature of the  $S_{11}(1535)$  has been its unusually large decay width to  $\eta N$ . We find strong evidence for a value at the high end of the PDG range. We believe our result because our model fully accounts for the threshold enhancement (cusp effect) due to the  $\eta N$  channel opening and the interference of the 2 overlapping resonances. Since no

other model has such a complete formulation, they can have model-dependent systematic errors as a result.

The properties of  $S_{11}(1650)$  are largely determined through the prominent bump in the elastic channel. The elastic  $T$  matrix has a peak in the imaginary part at about the right energy and the real part is decreasing at that energy; a strong resonance signal. The strongest inelastic signal comes in the  $\rho_3 N$  channel. The decay width to  $\eta N$  is small in this analysis, in agreement with previous analyses. The striking difference between branching fractions to  $\eta N$  has been another unusual feature of these states. The existence of the third  $S_{11}$  resonance is very weakly supported by the existing data. In our analysis, this state is most often determined by the need to fit non-statistical features in the partial wave amplitudes. Further data will be required to sort out the question of whether or not it exists.

The role of the inelastic  $\eta N$  channel is very important in the determination of resonance parameters for the  $S_{11}(1535)$  state, as shown in some detail in section IV. Unfortunately, the existing data for  $\pi N \rightarrow \eta N$  is sparse and of uncertain quality [29] (see Fig. 12). Recently published data [41] for  $\gamma p \rightarrow \eta N$  has been interpreted as evidence for a very large width ( $\simeq 200$  MeV). We do not include the Krusche *et al.* data in this analysis. However, very simple resonance models [41,42] were used to determine the large width. Since the large body of  $\pi N$  data was not fitted with their model, possible inconsistencies exist in their parameterization. Although the simple model has validity for the  $\eta N$  coupling to  $S_{11}(1535)$ , we feel there will still be significant effects from interference with  $S_{11}(1650)$  and coupled channel effects (e.g.  $\gamma N \rightarrow S_{11}(1650) \rightarrow \pi N \rightarrow S_{11}(1535) \rightarrow \eta N$ ).

#### D. Observables

$T$ -matrix amplitudes were fit using the Pitt-ANL model. We do not fit directly to data; rather, we fit the partial wave amplitudes. It is then interesting to compare the actual experimental data to our calculated observables to verify that nothing has been lost by not fitting to the actual data points.

The  $f$  and  $g$  spin non-flip and spin flip amplitudes are defined in terms of the Pitt-ANL  $T$ -matrix elements for  $\pi N$  elastic scattering by [43]:

$$\begin{aligned} f(\theta) &= \frac{1}{q} \sum_{\ell=0}^{\infty} [(\ell+1)T_{\ell+} + \ell T_{\ell-}] P_{\ell}(\cos \theta) \\ g(\theta) &= \frac{1}{q} \sum_{\ell=1}^{\infty} (T_{\ell+} - T_{\ell-}) P'_{\ell}(\cos \theta) \end{aligned} \quad (39)$$

where  $P_{\ell}$  and  $P'_{\ell}$  are the Legendre polynomials and their first derivative with respect to  $\cos \theta$ , respectively. The  $T_{\ell\pm}$  are the amplitudes for a particular  $\pi N$  scattering charge channel, where the  $\ell\pm$  refers to the total spin  $J = \ell \pm \frac{1}{2}$ , and  $q$  is the center of mass momentum of the final state pion. The  $T_{\ell\pm}$  are defined by Eq. (1) for the  $\pi N \rightarrow \pi N$  channel.

The differential cross section ( $\frac{d\sigma}{d\Omega}$ ) and polarization  $P$  are:

$$\begin{aligned} \frac{d\sigma}{d\Omega} &= |f(\theta)|^2 + |\sin \theta g(\theta)|^2 \\ \frac{d\sigma}{d\Omega} P &= 2\Im m [f(\theta)g^*(\theta)] \sin \theta \end{aligned} \quad (40)$$

Figure 13 shows a plot of the total cross section vs. the Pitt-ANL calculation for the process  $\pi^- p \rightarrow \pi^0 n$ . Figure 14 shows plots of the differential cross section,  $\frac{d\sigma}{d\Omega}$ , at a number of different energies for the process  $\pi^+ p \rightarrow \pi^+ p$ . Figure 15 shows plots of the nucleon recoil polarization,  $P$ , for a number of different energies for the process  $\pi^- p \rightarrow \pi^- p$ . In each case, the calculation using final fit parameters is in good agreement with the data. For the  $P$  data, the error bars are sometimes large.

For the plot in figures 13, 14, and 15 the data is taken from VPI's SAID database. It is a large collection of scattering data for a number of different reaction channels, including  $\pi N$  elastic and charge exchange reactions.

Based on our studies, we can conclude that our resonance parameters are very close to what would have been obtained if the fit had been made to the original data.

## VI. CONCLUSIONS

We have presented a new study of excitation of baryon resonances through pion-nucleon interactions. An expanded version of the Carnegie-Mellon Berkeley (CMB) was used in this

work. We added the  $\eta N$  channel to the calculation and used the latest data sets. The model satisfies many of the desirable theoretical constraints- two and three body unitarity, time reversal invariance, and analyticity. Because the model is based on a separable interaction, it is linked to a Hamiltonian approach, unlike many of the models previously used [2,4]. The model has a key feature of allowing large numbers of asymptotic channels and more than one resonance per partial wave. Since analyticity is satisfied and all inelastic thresholds are included, structure in the physical observables due to nonresonant effects are carefully treated. Resonances can then be found as poles in the complex  $s$  plane. As in the original CMB model, non-resonant processes are included as very wide resonances at very high or very low energies which are then subject to the same threshold effects as the resonances. This empirical approach is well established in potential scattering theory, but could be replaced later by theoretical calculations based on meson exchange models, e.g. [44].

Rather than deal with the complexities of a direct fit to the cross section and polarization data, we use the partial wave amplitudes of the VPI and KSU groups [2,25] and our own fit to the  $\pi N \rightarrow \eta N$  data. A re-evaluation of the  $\pi N \rightarrow \pi\pi N$  data is in progress by our group.

The features of this model are expected to be very important in the  $S_{11}$  partial wave where there are two overlapping resonances at 1535 and 1650 MeV and a strong threshold opening. The lower state pole and the  $\eta N$  channel opening close together and the quantum mechanical interference of the two states is found to be significant. We show how the interpretation of these states has very strong model dependence and how relaxing the features of the present model can skew the fitting results for the width and branching fractions to  $\pi N$  and  $\eta N$ . We get a new result for the branching fraction to  $\eta N$  at the high end of what has been previously published for  $S_{11}(1535)$ , making its characteristics even more unusual.

The general fitting results are presented in Tables VII and VIII. We searched for the same states seen in the previous analysis of Manley and Saleski [4]. This simplification was made because the data quality wasn't high enough for a valid search for weakly excited states. Although values of  $\chi^2/datapoint$  are roughly 2 for elastic fits, they are 10 or more for fits to the  $\pi N \rightarrow \pi\pi N$   $T$  matrix data. This is perhaps due to the lack of a treatment of correlations

in the error analysis of the pion production data. Modern experimental techniques could greatly improve the inelastic data set. We strongly encourage new measurements of the inelastic channels. A significant effort was made to determine error bars reflecting both the estimated errors in the  $T$  matrices used in the fits and the differing choices of background energy dependence.

We find strong and isolated states (e.g.  $P_{33}(1232)$  and  $D_{15}(1675)$ ) with very similar parameters as previous analyses. [2,4,3,6]. States with strong model dependence such as  $S_{11}(1535)$  or with significant changes in the data set such as  $S_{31}(1900)$  and  $D_{13}(1700)$  get quite different results. We find a full width of  $S_{11}(1535)$  at the low end of the range of previous values, especially with respect to the interpretations of recent  $\gamma p \rightarrow \eta p$  data [41]. The results presented here do not include the photoproduction data; rather, the present results are dependent on a fairly weak data set for  $\pi^- p \rightarrow \eta n$ . Nevertheless, the large widths obtained in analyses highly dependent on the Mainz eta photoproduction data are only loosely coupled to the large data set used in this study.

We are in the process of further extending the model to include photoproduction and electroproduction reactions. The Born terms are included for production of pions and etas and the resonance spectrum is being refit. Results of the present paper will then be subject to change.

## VII. ACKNOWLEDGMENTS

We are grateful to R. Arndt, R. Workman, and M. Manley for sharing their partial wave data and their analysis results with us. We have also benefited greatly from the programming and database work of D. Ciarletta, J. DeMartino, J. Greenwald, D. Kokales, M. Mihalcin, and K. Bordonaro at the University of Pittsburgh. Special thanks go to C. Tanase for investigating the analytic structure of this model in detail.

## TABLES

TABLE I. Model parameters for a *test* calculation in the  $S_{11}$  partial wave. These are the bare mass, the physical mass and width, and the dressed pole location for the two resonances included in the calculation. No background contributions are included.

state	bare mass (MeV)	physical mass (MeV)	full width (MeV)	physical pole (GeV)
$S_{11}(1535)$	1500	1518	83	1.507-0.032i
$S_{11}(1650)$	1650	1680	200	1.676-0.101i

TABLE II. Model parameters for *test* calculation in the  $S_{11}$  partial wave. These are the coupling parameters and branching fractions (b.f.) between the two asymptotic channels and the two resonances included in the calculation. No background contributions are included.

state	$\gamma_{\pi N}$ (GeV)	$\gamma_{\eta N}$ (GeV)	$\pi N$ b.f. (%)	$\eta N$ b.f. (%)
$S_{11}(1535)$	0.5	0.85	42	58
$S_{11}(1650)$	0.9	-0.04	96	4

TABLE III. Channels included in this analysis. Since isospin symmetry is assumed to simplify the analysis, all charge states of a particle have the same mass. We choose channels very similar to those used by KSU with identical nomenclature. All channels used in fits have fixed spin, orbital, and total angular momentum. In the text, the  $\rho N$  channel is denoted by  $(\rho_s N)_\ell$  with  $s$  equal to twice the total spin of the  $\rho N$  system and  $\ell$  giving the orbital angular momentum in spectroscopic notation. The orbital angular momentum of the  $\pi\Delta$  is also ambiguous, so it is also given as a subscript.

channel	baryon		meson	
	mass	width	mass	width
$\pi N$	939		139	
$\eta N$	939		549	
$\rho N$	939		770	153
$\sigma N$	939		800	800
$\omega N$	939		782	
$\pi\Delta$	1232	115	139	
$\pi N^*$	1440	200	139	
$K\Lambda$	1116		498	

TABLE IV. Model dependence for the  $S_{11}(1535)$ . See text for details.

Unitarity	Disp.	Res.	Channels	Mass	Width	$\pi N$	$\eta N$	$\pi\pi N$
	Rel.	Type	in fit	MeV	MeV	%	%	%
K-Matrix	NO	NRBW	$\pi N$	1518	87	43	6	51
K-Matrix	NO	NRBW	$\pi N, \eta N$	1532	108	45	39	16
K-Matrix	NO	NRBW	ALL	1535	126	42	44	14
K-Matrix	NO	RBW	$\pi N$	1514	84	35	0	65
K-Matrix	NO	RBW	$\pi N, \eta N$	1533	110	44	40	16
K-Matrix	NO	RBW	ALL	1534	125	42	43	15
Dyson eq.	YES	RBW	$\pi N$	1531	72	16	62	22
Dyson eq.	YES	RBW	$\pi N, \eta N$	1526	114	36	41	23
Dyson eq.	YES	RBW	ALL	1542	112	35	51	14

 TABLE V. Model dependence for the  $S_{11}(1650)$ . See text for details.

Unitarity	Disp.	Res.	Channels	Mass	Width	$\pi N$	$\eta N$	$\pi\pi N$
	Rel.	Type	in fit	MeV	MeV	%	%	%
K-Matrix	NO	NRBW	$\pi N$	1645	233	35	49	16
K-Matrix	NO	NRBW	$\pi N, \eta N$	1689	225	67	31	2
K-Matrix	NO	NRBW	ALL	1694	259	72	16	12
K-Matrix	NO	RBW	$\pi N$	1682	161	78	5	17
K-Matrix	NO	RBW	$\pi N, \eta N$	1692	233	75	15	10
K-Matrix	NO	RBW	ALL	1690	229	65	25	10
Dyson eq.	YES	RBW	$\pi N$	1692	138	65	35	0
Dyson eq.	YES	RBW	$\pi N, \eta N$	1676	104	54	45	1
Dyson eq.	YES	RBW	ALL	1689	202	74	6	20

TABLE VI.  $S_{11}$  Resonance parameters from fits to different elastic data sets. All results use the  $\pi N \rightarrow \eta N$  and  $\pi N \rightarrow \pi\pi N$  partial wave amplitudes as in the full analysis. Comparisons are made for results using the VPI and a mixture of the CMB80 and KH80 elastic partial wave amplitudes (as was done in Ref. [4]). The first two lines in the table give results for  $S_{11}(1535)$  and the last two lines give results for  $S_{11}(1650)$ . Although all channels were used in the fit, only the total  $\pi\pi N$  branching fraction is given.

Elastic	Mass	Width	$\pi N$ b.f.	$\eta N$ b.f.	$\pi\pi N$ b.f.
Data Set	MeV	MeV	%	%	%
VPI	1542	112	35	51	14
CMB/KH80	1535	137	35	53	12
VPI	1689	202	74	6	20
CMB/KH80	1691	222	58	15	27

TABLE VII. Results for masses, full widths, and elastic fractions for all resonances found in this analysis. All resonances found in the KSU analysis were searched for, but not all were found. No attempt was made to find new resonances because then data quality is not good enough for a new search. See text for more details.

Resonance	Mass (MeV)	Width (MeV)	Elasticity %	Reference
S <sub>11</sub> (1535)	1542(3)	112(19)	35(8)	Pitt-ANL
****	1534(7)	151(27)	51(5)	KSU
	1520-1555	100-250	35-55	PDG
	1550(40)	240(80)	50(10)	CMB
S <sub>11</sub> (1650)	1689(12)	202(40)	74(2)	Pitt-ANL
****	1659(9)	173(12)	89(7)	KSU
	1640-1680	145-190	55-90	PDG
	1650(30)	150(40)	65(10)	CMB
S <sub>11</sub> (2090)	1822(43)	248(185)	17(3)	Pitt-ANL
*	1928(59)	414(157)	10(10)	KSU
	≈ 2090			PDG
	2180(80)	350(100)	18(8)	CMB
P <sub>11</sub> (1440)	1479(80)	490(120)	72(5)	Pitt-ANL
****	1462(10)	391(34)	69(3)	KSU
	1430-1470	250-450	60-70	PDG
	1440(30)	340(70)	68(4)	CMB
P <sub>11</sub> (1710)	1699(65)	143(100)	27(13)	Pitt-ANL

***	1717(28)	478(226)	9(4)	KSU
	1680-1740	50-250	10-20	PDG
	1700(50)	90(30)	20(4)	CMB
P <sub>11</sub> (2100)	2084(93)	1077(643)	2(5)	Pitt-ANL
*	1885(30)	113(44)	15(6)	KSU
	≈ 2100			PDG
	2125(75)	260(100)	12(3)	CMB
P <sub>13</sub> (1720)	1716(112)	121(39)	5(5)	Pitt-ANL
****	1717(31)	383(179)	13(5)	KSU
	1650-1750	100-200	10-20	PDG
	1700(50)	125(70)	10(4)	CMB
D <sub>13</sub> (1520)	1518(3)	124(4)	63(2)	Pitt-ANL
****	1524(4)	124(8)	59(3)	KSU
	1515-1530	110-135	50-60	PDG
	1525(10)	120(15)	58(3)	CMB
D <sub>13</sub> (1700)	1736(33)	175(133)	4(2)	Pitt-ANL
***	1737(44)	249(218)	1(2)	KSU
	1650-1750	50-150	5-15	PDG
	1675(25)	90(40)	11(5)	CMB
D <sub>13</sub> (2080)	2003(18)	1070(858)	13(3)	Pitt-ANL
**	1804(55)	447(185)	23(3)	KSU
	≈ 2080			PDG

	2060(80)	300(100)	14(7)	CMB
D <sub>15</sub> (1675)	1685(4)	131(10)	35(1)	Pitt-ANL
****	1676(2)	159(7)	47(2)	KSU
	1670-1685	140-180	40-50	PDG
	1675(10)	160(20)	38(5)	CMB
F <sub>15</sub> (1680)	1679(3)	128(9)	69(2)	Pitt-ANL
****	1684(4)	139(8)	70(3)	KSU
	1675-1690	120-140	60-70	PDG
	1680(10)	120(10)	62(5)	CMB
F <sub>17</sub> (1990)	2311(16)	205(72)	22(11)	Pitt-ANL
**	2086(28)	535(117)	6(2)	KSU
	≈ 1990			PDG
	1970(50)	350(120)	6(2)	CMB
G <sub>17</sub> (2190)	2168(18)	453(101)	20(4)	Pitt-ANL
****	2127(9)	547(48)	22(1)	KSU
	2100-2200	350-550	10-20	PDG
	2200(70)	500(150)	12(6)	CMB
S <sub>31</sub> (1620)	1617(15)	143(42)	45(5)	Pitt-ANL
****	1672(7)	154(37)	9(2)	KSU
	1615-1675	120-180	20-30	PDG
	1620(20)	140(20)	25(3)	CMB

S <sub>31</sub> (1900)	1802(87)	48(45)	33(10)	Pitt-ANL
***	1920(24)	263(39)	41(4)	KSU
	1850-1950	140-240	10-30	PDG
	1890(50)	170(50)	10(3)	CMB
P <sub>31</sub> (1750)	1721(61)	70(50)	6(9)	Pitt-ANL
*	1744(36)	299(118)	8(3)	KSU
	≈ 1750			PDG
P <sub>31</sub> (1910)	1995(12)	713(465)	29(21)	Pitt-ANL
****	1882(10)	239(25)	23(8)	KSU
	1870-1920	190-270	15-30	PDG
	1910(40)	225(50)	19(3)	CMB
P <sub>33</sub> (1232)	1234(5)	112(18)	100(1)	Pitt-ANL
****	1231(1)	118(4)	100(0)	KSU
	1230-1234	115-125	98-100	PDG
	1232(3)	120(5)	100(0)	CMB
P <sub>33</sub> (1600)	1687(44)	493(75)	28(5)	Pitt-ANL
***	1706(10)	430(73)	12(2)	KSU
	1550-1700	250-450	10-25	PDG
	1600(50)	300(100)	18(4)	CMB
P <sub>33</sub> (1920)	1889(100)	123(53)	5(4)	Pitt-ANL
***	2014(16)	152(55)	2(2)	KSU
	1900-1970	150-300	5-20	PDG

	1920(80)	300(100)	20(5)	CMB
D <sub>33</sub> (1700)	1732(23)	119(70)	5(1)	Pitt-ANL
****	1762(44)	599(248)	14(6)	KSU
	1670-1770	200-400	10-20	PDG
	1710(30)	280(80)	12(3)	CMB
D <sub>35</sub> (1930)	1932(100)	316(237)	9(8)	Pitt-ANL
***	1956(22)	526(142)	18(2)	KSU
	1920-1970	250-450	5-20	PDG
	1940(30)	320(60)	14(4)	CMB
D <sub>35</sub> (2350)	2459(100)	480(360)	7(14)	Pitt-ANL
*	2171(18)	264(51)	2(0)	KSU
	≈ 2350			PDG
	2400(125)	400(150)	20(10)	CMB
F <sub>35</sub> (1752)	1724(61)	138(68)	0(1)	Pitt-ANL
*	1752(32)	251(93)	2(1)	KSU
F <sub>35</sub> (1905)	1873(77)	461(111)	9(1)	Pitt-ANL
****	1881(18)	327(51)	12(3)	KSU
	1870-1920	280-440	5-15	PDG
	1910(30)	400(100)	8(3)	CMB
F <sub>37</sub> (1950)	1936(4.5)	245(12)	44(1)	Pitt-ANL
****	1945(2)	300(7)	38(1)	KSU

1940-1960

290-350

35-40

PDG

1950(15)

340(50)

39(4)

CMB



TABLE VIII. Results for decay branching ratios of all resonances found in this analysis. Fractions are expressed as a percentage of the full width found in table VII.

Resonance	Channel	Pitt-ANL	KSU	PDG
S <sub>11</sub> (1535)	$\pi N$	35(4)	51(5)	35-55
	$\eta N$	51(5)	43(6)	30-55
	$\rho_1 N$	2(1)	2(1)	0-4
	$(\rho_3 N)_D$	0(1)	1(1)	
	$(\pi \Delta)_D$	1(1)	0(0)	0-1
	$(\sigma N)_P$	2(1)	1(1)	0-3
	$\pi N^*(1440)$	10(9)	2(2)	0-7
S <sub>11</sub> (1650)	$\pi N$	74(2)	89(7)	55-90
	$\eta N$	6(1)	3(5)	3-10
	$\rho_1 N$	1(1)	0(0)	4-14
	$(\rho_3 N)_D$	13(3)	3(2)	
	$(\pi \Delta)_D$	2(1)	2(1)	3-7
	$(\sigma N)_P$	1(1)	2(2)	0-4
	$\pi N^*(1440)$	3(1)	1(1)	0-5
S <sub>11</sub> (2090)	$\pi N$	17(7)	10(10)	
	$\eta N$	41(4)	0(3)	
	$\rho_1 N$	36(1)	49(22)	
	$(\rho_3 N)_D$	1(1)	0(1)	
	$(\pi \Delta)_D$	1(1)	6(14)	
	$(\sigma N)_P$	2(1)	4(10)	
	$\pi N^*(1440)$	2(1)	30(22)	

P <sub>11</sub> (1440)	$\pi\text{N}$	72(2)	69(3)	60-70
	$\eta\text{N}$	0(1)		0-8
	$\rho_1\text{N}$	0(1)		
	$(\pi\Delta)_P$	16(1)	22(3)	20-30
	$(\sigma\text{N})_S$	12(1)	9(2)	5-10
	$\text{K}\Lambda$	0(1)		
P <sub>11</sub> (1710)	$\pi\text{N}$	27(4)	9(4)	10-20
	$\eta\text{N}$	6(1)		
	$\rho_1\text{N}$	17(1)	3(7)	5-25
	$(\pi\Delta)_P$	39(8)	49(10)	15-40
	$(\sigma\text{N})_S$	1(1)	2(4)	10-40
	$\text{K}\Lambda$	10(10)	37(10)	5-25
P <sub>11</sub> (2100)	$\pi\text{N}$	2(1)	15(6)	
	$\eta\text{N}$	61(61)		
	$\rho_1\text{N}$	4(1)	27(79)	
	$(\pi\Delta)_P$	2(1)	24(18)	
	$(\sigma\text{N})_S$	10(1)	32(71)	
	$\text{K}\Lambda$	21(20)	2(6)	
P <sub>13</sub> (1720)	$\pi\text{N}$	5(5)	13(5)	10-20
	$\eta\text{N}$	4(1)		
	$\rho_1\text{N}$	91(1)	87(5)	70-85
	Flux	0(1)		

D <sub>13</sub> (1520)	$\pi N$	63(1)	59(3)	50-60
	$\eta N$	0(1)		
	$(\rho_3 N)_S$	9(1)	21(4)	15-25
	$(\pi \Delta)_D$	11(2)	15(4)	5-12
	$(\pi \Delta)_S$	15(2)	5(3)	10-14
	$(\sigma N)_P$	1(1)		0-8
D <sub>13</sub> (1700)	$\pi N$	4(1)	1(2)	5-15
	$\eta N$	0(1)		
	$(\rho_3 N)_S$	7(1)	13(17)	0-35
	$(\pi \Delta)_D$	79(56)	80(19)	
	$(\pi \Delta)_S$	11(1)	5(10)	
	$(\sigma N)_P$	0(1)	2(4)	
D <sub>13</sub> (2080)	$\pi N$	13(2)	23(3)	
	$\eta N$	0(2)		
	$(\rho_3 N)_S$	6(6)	26(14)	
	$(\pi \Delta)_D$	17(10)	21(14)	
	$(\pi \Delta)_S$	40(10)	3(7)	
	$(\sigma N)_P$	24(24)	27(12)	
D <sub>15</sub> (1675)	$\pi N$	35(2)	47(2)	40-50
	$\eta N$	0(1)		
	$\rho_1 N$	0(1)	0(0)	1-3
	$(\rho_3 N)_D$	1(1)	0(0)	
	$(\pi \Delta)_D$	63(2)	53(2)	50-60

F <sub>15</sub> (1680)	$\pi N$	69(1)	70(3)	60-70
	$\eta N$	0(1)		
	$(\rho_3 N)_F$	3(1)	2(1)	1-5
	$(\rho_3 N)_P$	5(1)	5(3)	0-12
	$(\pi \Delta)_F$	1(1)	1(1)	0-2
	$(\pi \Delta)_P$	14(3)	10(3)	6-14
	$(\sigma N)_D$	9(1)	12(3)	5-20
F <sub>17</sub> (1990)	$\pi N$	22(3)	6(2)	
	$\eta N$	0(1)	94(2)	
	Flux	77(77)		
G <sub>17</sub> (2190)	$\pi N$	20(1)	22(1)	10-20
	$\eta N$	0(1)		
	$(\rho_3 N)_D$	29(28)	29(6)	
	$(\omega_3 N)_D$	51(51)	49(7)	
S <sub>31</sub> (1620)	$\pi N$	45(1)	9(2)	20-30
	$\rho_1 N$	14(3)	25(6)	7-25
	$(\rho_3 N)_D$	2(1)	4(3)	
	$(\pi \Delta)_D$	39(2)	62(6)	30-60
	$\pi N^*(1440)$	0(1)		
S <sub>31</sub> (1900)	$\pi N$	33(6)	41(4)	10-30
	$\rho_1 N$	30(2)	5(7)	
	$(\rho_3 N)_D$	5(1)	33(10)	
	$(\pi \Delta)_D$	28(1)	16(8)	

	$\pi N^*(1440)$	4(1)	6(9)	
P <sub>31</sub> (1750)	$\pi N$	6(6)	8(3)	
	$\pi N^*(1440)$	83(1)	28(9)	
	Flux	11(11)	64(9)	
P <sub>31</sub> (1910)	$\pi N$	29(29)	23(8)	15-30
	$\pi N^*(1440)$	56(7)	67(10)	
	Flux	15(15)	10(1)	
P <sub>33</sub> (1232)	$\pi N$	100(1)	100(0)	98-100
	$(\pi\Delta)_P$	0(1)	0(0)	
	$\pi N^*(1440)$	0(1)	0(0)	
P <sub>33</sub> (1600)	$\pi N$	28(5)	12(2)	10-25
	$(\pi\Delta)_P$	59(10)	67(5)	40-70
	$\pi N^*(1440)$	13(4?1)	20(4)	10-35
P <sub>33</sub> (1920)	$\pi N$	5(61?)	2(2)	5-20
	$(\pi\Delta)_P$	41(2.9)	83(26)	
	$\pi N^*(1440)$	53(8.2)	15(24)	
D <sub>33</sub> (1700)	$\pi N$	5(1.6)	14(6)	10-20
	$(\rho_3 N)_S$	1(1)	8(4)	5-20
	$(\pi\Delta)_D$	4(1)	4(3)	1-7
	$(\pi\Delta)_S$	90(1.7)	74(7)	25-50

D <sub>35</sub> (1930)	$\pi N$	9(8)	18(2)	5-20
	$K\Lambda$	91(11)		
	Flux		82(2)	
D <sub>35</sub> (2350)	$\pi N$	7(14)	2(0)	
	$K\Lambda$	93(15)		
	Flux		98(0)	
F <sub>35</sub> (1752)	$\pi N$	0(1)	2(1)	
	$(\rho_3 N)_P$	60(60)	22(14)	
	$(\pi \Delta)_F$	40(1)	48(16)	
	$(\pi \Delta)_P$	0(1)	28(18)	
F <sub>35</sub> (1905)	$\pi N$	9(2.2)	12(3)	5-15
	$(\rho_3 N)_P$	24(1)	86(3)	0-60
	$(\pi \Delta)_F$	44(1)	0(1)	0-25
	$(\pi \Delta)_P$	23(1)	1(3)	
F <sub>37</sub> (1950)	$\pi N$	44(1)	38(1)	35-40
	$(\rho_3 N)_F$		43(1)	0-10
	$(\pi \Delta)_F$	36(1)	18(3)	20-30
	Flux	20(20)		

---



---

TABLE IX. Pole positions. The complex energy of the pole for each state is given along with the physical mass.

Resonance	Res Mass (MeV)	Pole Position (MeV)
S <sub>11</sub> (1535)	1545	1525 - 51 i
S <sub>11</sub> (1650)	1693	1663 - 120 i
S <sub>11</sub> (2090)	1822	1795 - 110 i
P <sub>11</sub> (1440)	1479	1383 - 158 i
P <sub>11</sub> (1710)	1699	1679 - 66 i
P <sub>11</sub> (2100)	2083	1810 - 311 i
P <sub>13</sub> (1720)	1716	1692 - 47 i
D <sub>13</sub> (1520)	1520	1504 - 56 i
D <sub>13</sub> (1700)	1729	1704 - 78 i
D <sub>13</sub> (2080)	2002	1824 - 307 i
D <sub>15</sub> (1675)	1687	1674 - 60 i
F <sub>15</sub> (1680)	1679	1667 - 61 i
F <sub>17</sub> (1990)	2311	2301 - 101 i
G <sub>17</sub> (2190)	2168	2107 - 190 i
S <sub>31</sub> (1620)	1633	1607 - 74 i
S <sub>31</sub> (1900)	1798	1795 - 29 i
P <sub>31</sub> (1750)	1721	1714 - 34 i
P <sub>31</sub> (1910)	1995	1880 - 248 i
P <sub>33</sub> (1232)	1234	1217 - 48 i
P <sub>33</sub> (1600)	1687	1599 - 156 i
P <sub>33</sub> (1920)	1889	1880 - 60 i
D <sub>33</sub> (1700)	1732	1726 - 59 i
D <sub>35</sub> (1930)	1932	1883 - 125 i

$D_{35}(2350)$	2459	2427 - 229 i
$F_{35}(1752)$	1724	1697 - 56 i
$F_{35}(1905)$	1873	1793 - 151 i
$F_{37}(1950)$	1936	1910 - 115 i

---

---

## FIGURES

FIG. 1. Schematic diagram for the Dyson equation iteration.

FIG. 2. Schematic diagram for the self energy ( $\Sigma$ ) iteration. Each resonance is allowed to couple to all open channels.

FIG. 3.  $\phi(s)$  (channel propagator) distributions for the  $\pi N$  and  $\eta N$  channels in  $S_{11}$  partial wave. These functions are used in the two channel-two resonance test case and in the final fits.

FIG. 4. One resonance-one channel test case  $T$  matrix (real and imaginary parts) using parameters appropriate for the  $P_{33}(1232)$  resonance. Solid dots are placed at the energy of the resonance mass.

FIG. 5. Self energy function,  $\Sigma_{1535,1535}$  for the test case where only  $\pi N$  and  $\eta N$  channels are included.

FIG. 6.  $T$  matrices for two channel-two resonance test case. The real and imaginary parts are shown for the  $\pi N \rightarrow \pi N$  and  $\pi N \rightarrow \eta N$  reactions. Solid dots are placed at the values of the resonance masses obtained from these  $T$  matrices.

FIG. 7. Best fit calculation for  $S_{11}$  partial wave at the  $\eta N$  threshold.  $T$  matrices for  $\pi N \rightarrow \pi N$  and  $\pi N \rightarrow \rho_1 N$  are shown.

FIG. 8.  $T$ -matrices for  $S_{11}$  partial wave for elastic scattering and final states of  $\rho_1 N$ ,  $\sigma N$ , and  $\pi N^*(1440)$  calculated with the full model using final fit parameters. The dotted line is calculated with only resonance couplings turned on and the dashed line is calculated with only non-resonant couplings enabled. The full calculation, which cannot be a sum of the dotted and dashed lines because the resonant and non-resonant diagrams interfere, is shown as a solid line.

FIG. 9.  $T$  matrices according to the best fit for the  $D_{15}$  partial wave. The VPI partial wave amplitudes are shown by data points with error bars. The KSU fit of Manley and Saleski is shown as dashed lines and the fit of this work is shown as solid lines.

FIG. 10.  $T$  matrices for  $D_{13}$  partial wave. The same labeling is used as in Fig. 9.

FIG. 11.  $T$  matrices for  $S_{11}$  partial wave. The same labeling is used as in Fig. 9.

FIG. 12. Total cross section for the  $\pi^-p \rightarrow \eta n$  reaction. The data was taken from sources in Ref. [27], leaving out the low energy Brown, *et al.* data. The solid line shows the total cross section calculated with the final fit result of this work using all partial waves. The contribution from the  $S_{11}$  partial wave would be very similar to the full result.

FIG. 13. Pitt-ANL model calculation using final fit compared with the total cross section for the process  $\pi^-p \rightarrow \pi^0 n$ . The fit was to  $T$ -matrix amplitudes derived in part from the data shown here. Data shown is from the VPI SAID database.

FIG. 14. Pitt-ANL model calculation using final fit parameters compared to the differential cross section for the process  $\pi^+p \rightarrow \pi^+p$ . Data from the VPI SAID database is shown.

FIG. 15. Pitt-ANL model calculation using final fit parameters of the polarization,  $P$ , for the process  $\pi^-p \rightarrow \pi^-p$ . Data from the VPI SAID database is shown.

## REFERENCES

- [1] Particle Data Group, Phys. Rev. D**54**, 1 (1996).
- [2] Richard A. Arndt, Igor I. Strakovsky, Ron L. Workman, and Marcello M. Pavan, Phys. Rev. C**52**, 2120 (1995).
- [3] G. Höhler, F. Kaiser, R. Koch, and E. Pietarinen, *Handbook of Pion-Nucleon scattering*, [Physics Data No. 12-1 (1979)].
- [4] D.M. Manley and E.M. Saleski, Phys. Rev. D**45**, 4002 (1992).
- [5] T. Feuster and U. Mosel, Phys. Rev. C**58**, 457 (1998).
- [6] R.E. Cutkosky, C.P. Forsyth, R.E. Hendrick, and R.L. Kelly, Phys. Rev. D**20**, 2839 (1979), R.E. Cutkosky, C.P. Forsyth, J.B. Babcock, R.L. Kelly, and R.E. Hendrick, in *Baryons 1980*, Proceedings of the IV International Conference on Baryon Resonances, ed. N. Isgur (University of Toronto, 1980), p. 19.
- [7] F. Foster and G. Hughes, Rep. Prog. Phys. **46**, 1445 (1983).
- [8] N. Isgur and G. Karl, Phys. Rev. D**18**, 4187 (1978); D**19**, 2653 (1979).
- [9] S. Capstick and N. Isgur, Phys. Rev. D**34**, 2809 (1986), S. Capstick and B. D. Keister, Phys. Rev. D**51**, 3598 (1995).
- [10] R. Bijker, F. Iachello, and A. Leviatan, Ann. Phys. (N.Y.), **236**, 69 (1994).
- [11] F. Cardarelli, E. Pace, G. Salme, and S. Simula, Phys. Lett. **B357**, 267 (1995).
- [12] G.E. Brown and M. Rho, Phys. Lett. **82B**, 177 (1979); G.E. Brown, M. Rho, and V. Vento, Phys. Lett **94B**, 383 (1979)
- [13] S. Theberg, A.W. Thomas, and G.A. Miller, Phys. Rev. D**22**, 2838 (1980);**24**, 216 (1981); D. H. Liu, A.W. Thomas, and A. G. Williams, Phys. Rev. C**55**, 3108 (1997)
- [14] Chr. V. Christov, *et al.*, Prog, Part. Nucl. Phys. **37**, 91 (1996); R. Alkofer, H. Reinhart,

- and H. Weigel, Phys. Rep. **265**, 139 (1996).
- [15] See review by L. Wilets, **Non-Topological Solitons**, (World Scientific, 1989).
- [16] Zhenping Li, Phys. Rev. D**50** (1994) 5639; A. Glozman and D. O. Riska, Phys. Rep. **268**, 263 (1996); P.-N. Shen, Y.-B. Dong, Z.-Y. Zhang, Y.-W. Yu, and T.-S. H. Lee, Phys. Rev. **C55**, 2024 (1997).
- [17] S. Capstick, Phys. Rev. D**46**, 2864 (1992).
- [18] Simon Capstick and Winston Roberts, Phys. Rev. D**47**, 1994 (1993), Phys. Rev. D**49**, 4570 (1994).
- [19] F. Butler, H. Chen, J. Sexton, A. Vaccarino, and D. Weingarten, Phys. Rev. Lett. **70**, 2849 (1993).
- [20] R.E. Cutkosky, R.E. Hendrick, J.W. Alcock, Y.A. Chao, R.G. Lipes, J.C. Sandusky, and R.L. Kelly, Phys. Rev. D**20**, 2804 (1979). R. Kelly and R.E. Cutkosky, Phys. Rev. D **20**, 2782 (1979).
- [21] R. Koch, Z. Phys. **C29**, 597 (1985), Nucl. Phys. **A448**, 707 (1986), R. Koch and E. Pietarinen, Nucl. Phys. **A336**, 331 (1980).
- [22] G. Höhler,  $\pi N$  Newsletter, G. Höhler, W. Kluge, and B.M.K. Nefkens, eds., **13**, 320 (1997).
- [23] R.G. Moorhouse, H. Oberlack, and A.H. Rosenfeld, Phys. Rev. D**9**, 1 (1974).
- [24] Ramesh Bhandari and Yung-An Chao, Phys. Rev. **D15**, 192, (1977).
- [25] D.M. Manley, R.A. Arndt, Y. Goradia, and V.L. Teplitz, Phys. Rev. D**30**, 904 (1984).
- [26] G. Höhler,  $\pi N$  Newsletter, G. Höhler, W. Kluge, and B.M.K. Nefkens, eds., **9**, 1 (1993).
- [27] M. Batinic, I. Slaus, A. Svarc, and B.M.K. Nefkens, Phys. Rev. **C51**, 2310 (1995).
- [28] R.M. Brown, et al., Nucl. Phys. **B153**, 89 (1979).

- [29] R. Clajus and B.M.K. Nefkens,  $\pi N$  Newsletter, G. Höhler, W. Kluge, and B.M.K. Nefkens, eds., **7**, 76 (1991).
- [30] T.P. Vrana, University of Pittsburgh Ph. D. thesis, unpublished.
- [31] William R. Frazer and Archibald W. Henry, Phys. Rev. **134**, B1307 (1964).
- [32] R.E. Cutkosky and S. Wang, Phys. Rev. D**42**, 235 (1990).
- [33] C. Deutsch-Sauermann, B. Friman, and W. Nörenberg, Phys. Lett. **B341**, 261 (1995), Phys. Lett. **B409**, 51 (1977).
- [34] M. Mulhearn and J. Mueller, private communication.
- [35] D.J. Herndon et al., Phys. Rev. D**11**, 3165 (1975) and R.L. Longacre et al., Phys. Rev. D**17**, 1795 (1978).
- [36] K.W.J. Barnham, in *Proceedings of the Topical Conference on Baryon Resonances*, R.T. Ross and D.H. Saxon, eds.; Univ. Press, London, 1976.
- [37] Ramesh Bhandari and Yung-An Chao, Phys. Rev. D**15**, 192 (1977).
- [38] M. Benmerrouche, Nimai C. Mukhopadhyay, and J.F. Zhang, Phys. Rev. D**51**, 3237 (1995).
- [39] L. Tiator, C. Bennhold, and S.S. Kamalov, Nucl. Phys. **A580**, 455 (1994).
- [40] Franz Gross and Yohanes Surya, Phys. Rev. C**47**, 703 (1993).
- [41] B. Krusche, et al., Phys. Rev. Lett. **74**, 3736 (1995).
- [42] B. Krusche, N. Mukhopadhyay, J.F. Zhang, and M. Benmerrouche, Phys. Lett. **B397**, 171 (1997).
- [43] M.L. Goldberger and K.M. Watson, *Collision Theory*, John Wiley and Sons, Inc., 1967.
- [44] T. Sato and T.-S. H. Lee, Phys. Rev. C**54**, 2660 (1996).

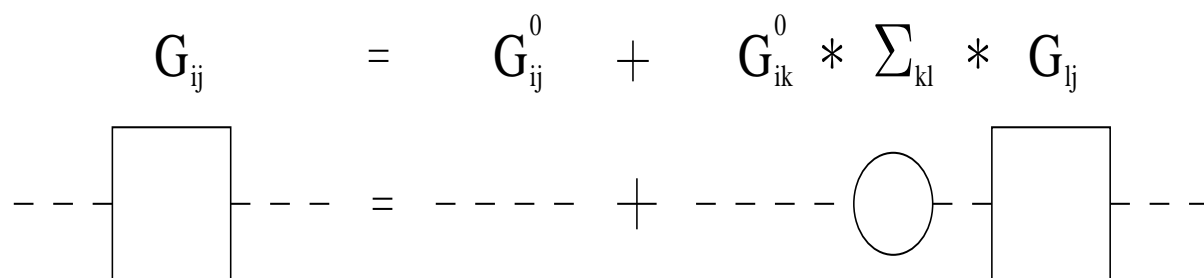


Fig 1

T.P. Vrana, S.A. Dytman, + T.-S. H. Lee

Baryon Resonance Extraction ...

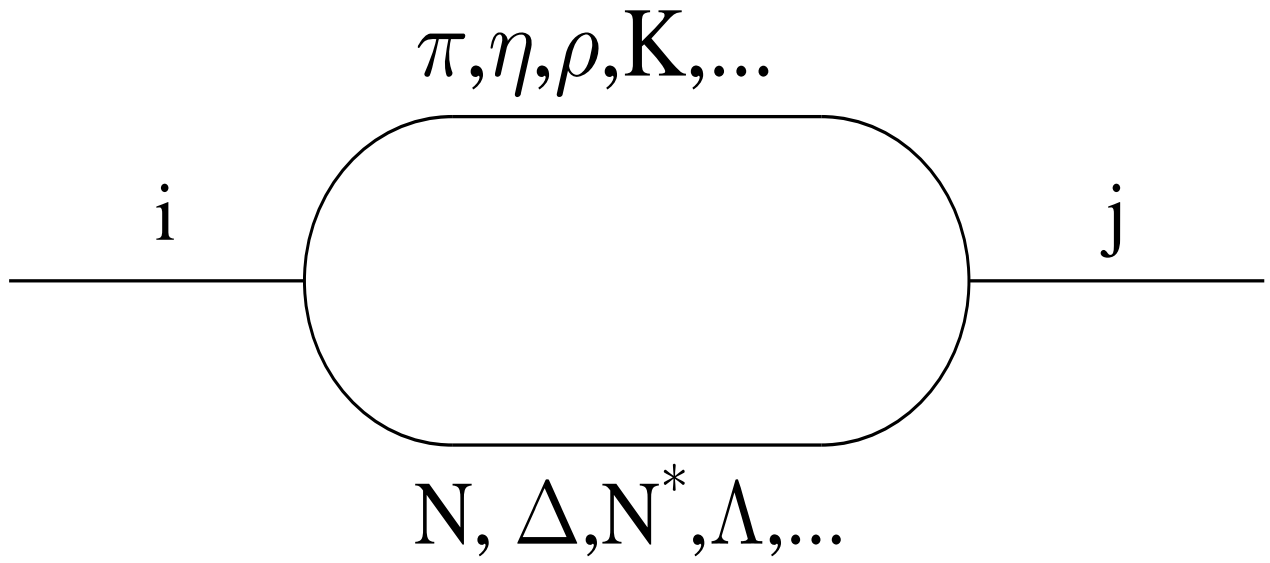


Fig 2

T.P. Vrana, S.A. Dytman, + T.-S. H. Lee

Baryon Resonance Extraction ...

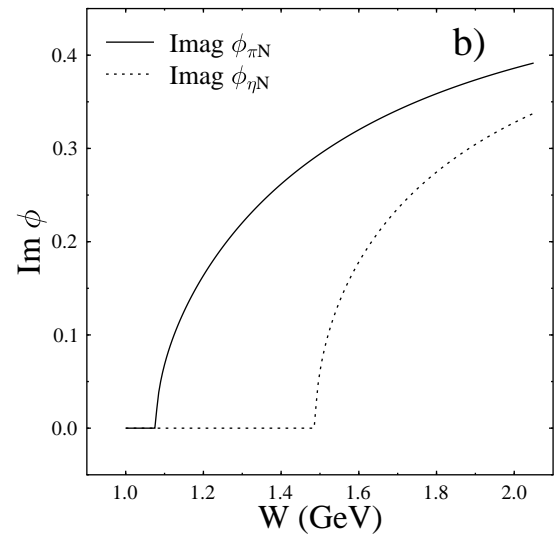
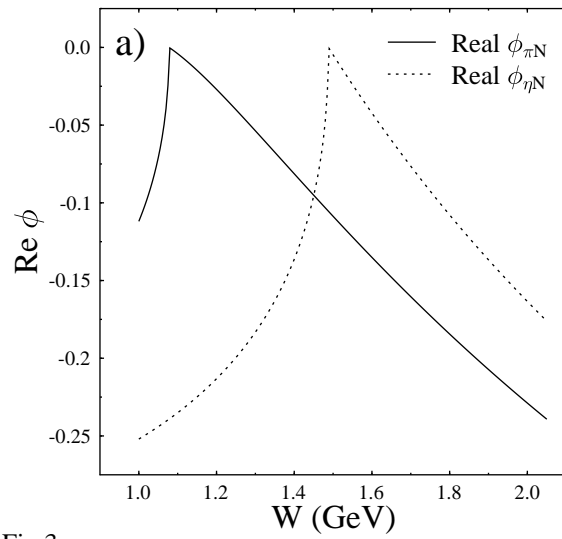


Fig 3  
 T.P. Vrana, S.A. Dytman, + T.-S. H. Lee  
 Baryon Resonance Extraction ...

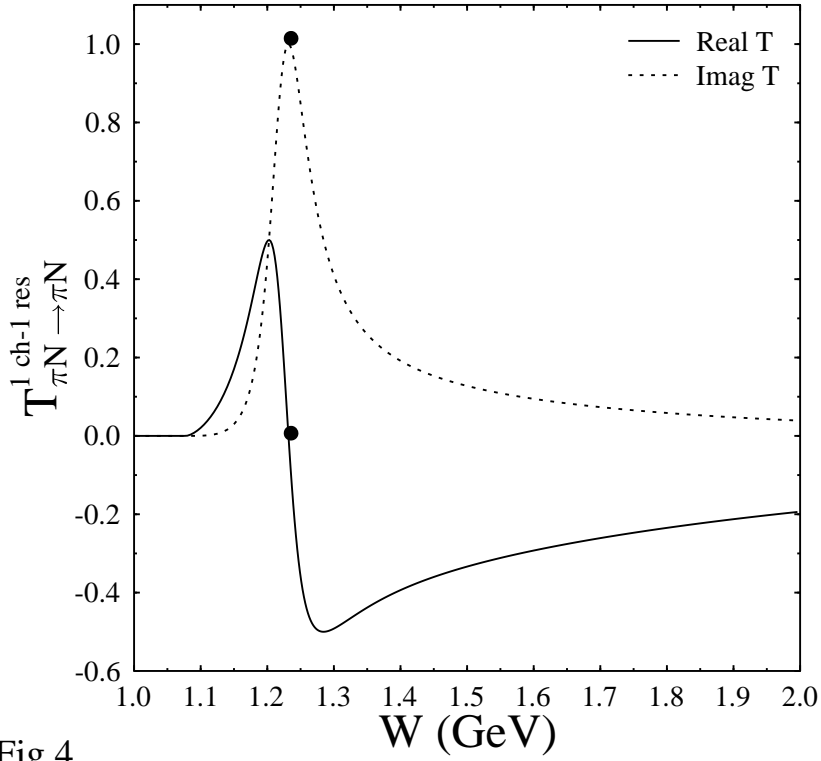


Fig 4

T.P. Vrana, S.A. Dytman, + T.-S. H. Lee

Baryon Resonance Extraction ...

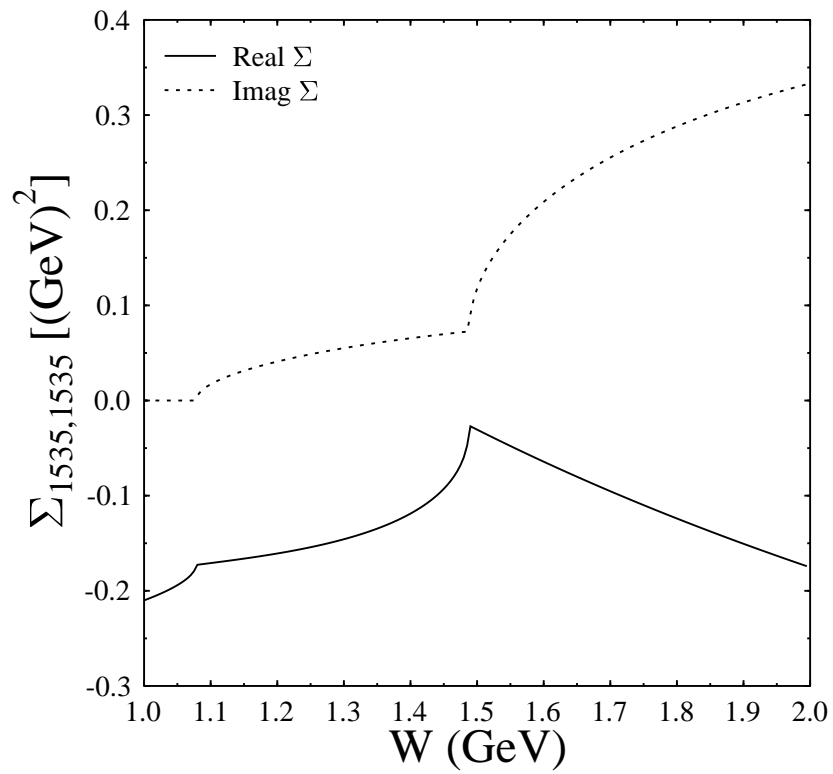


Fig 5

T.P. Vrana, S.A. Dytman, + T.-S. H. Lee

Baryon Resonance Extraction ...

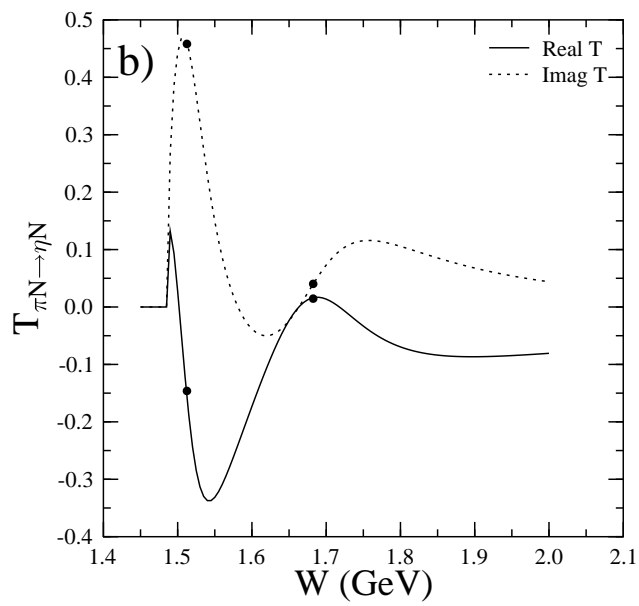
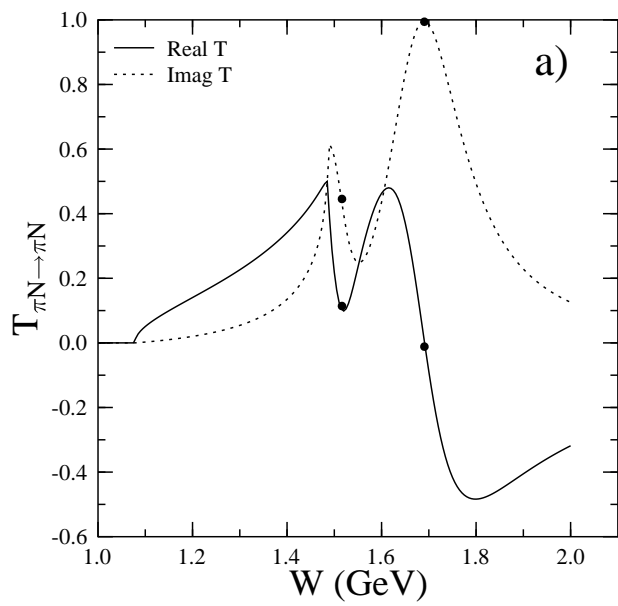


Fig 6  
 T.P. Vrana, S.A. Dytman, + T.-S. H. Lee  
 Baryon Resonance Extraction ...

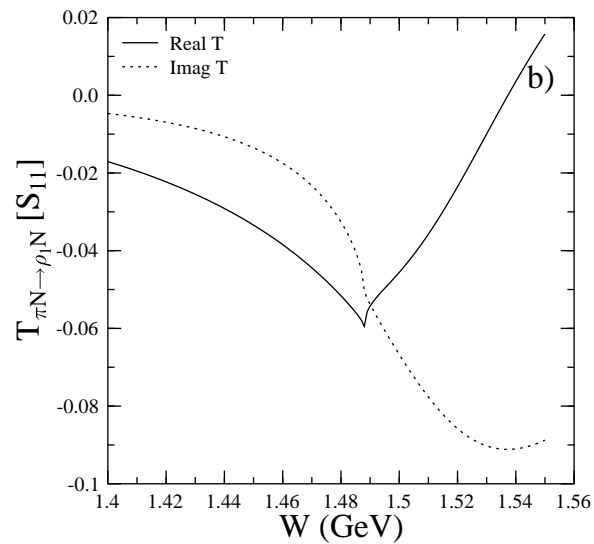
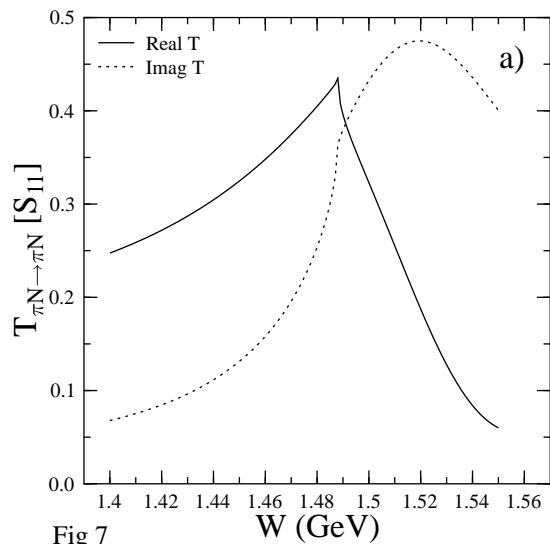


Fig 7  
 T.P. Vrana, S.A. Dytman, + T.-S. H. Lee  
 Baryon Resonance Extraction ...

This figure "fig8\_c.gif" is available in "gif" format from:

<http://arxiv.org/ps/nucl-th/9910012v2>

This figure "fig9\_c.gif" is available in "gif" format from:

<http://arxiv.org/ps/nucl-th/9910012v2>

This figure "fig10\_c.gif" is available in "gif" format from:

<http://arxiv.org/ps/nucl-th/9910012v2>

This figure "fig11\_c.gif" is available in "gif" format from:

<http://arxiv.org/ps/nucl-th/9910012v2>

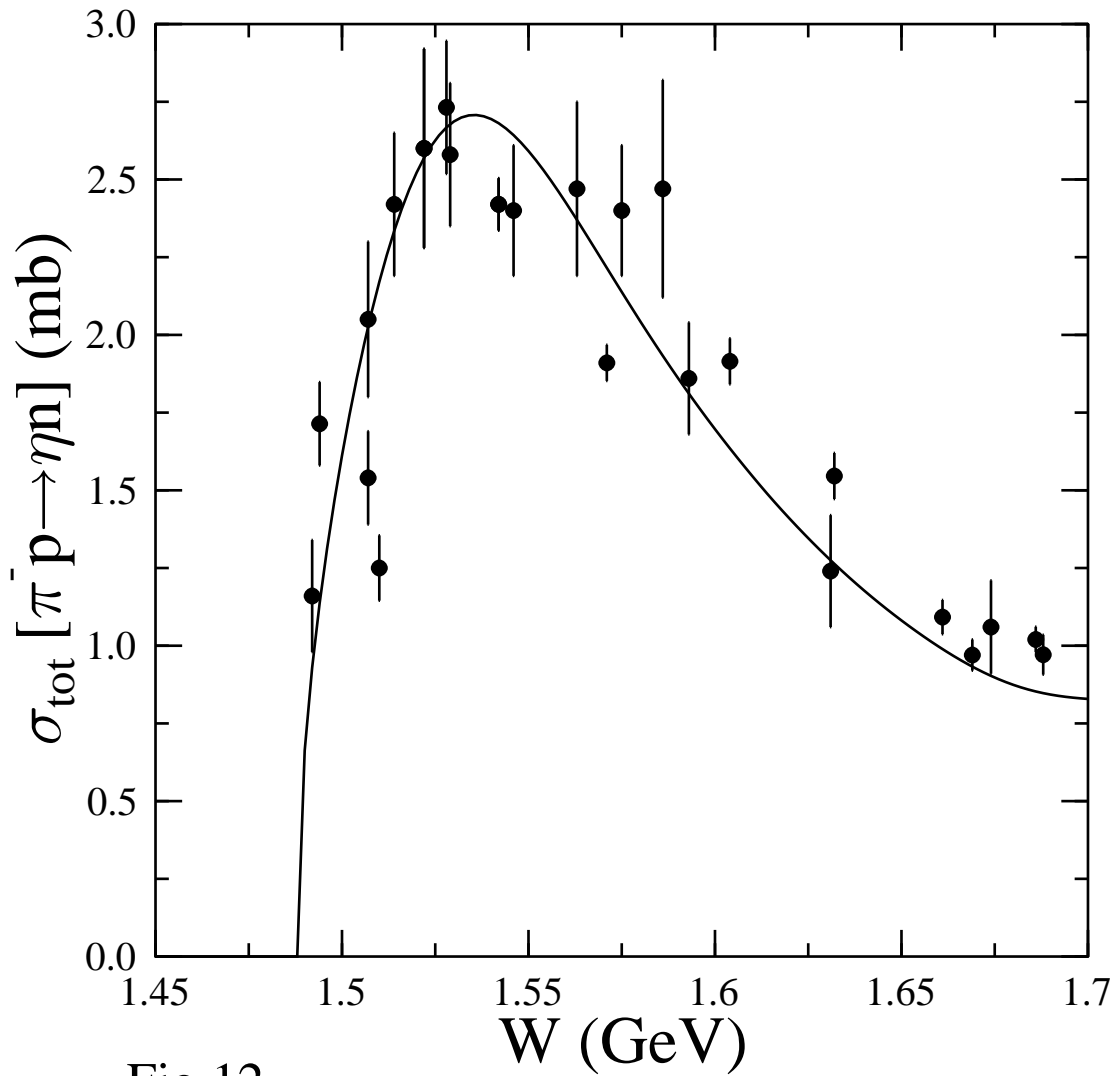


Fig 12

T.P. Vrana, S.A. Dytman, + T.-S. H. Lee  
Baryon Resonance Extraction ...

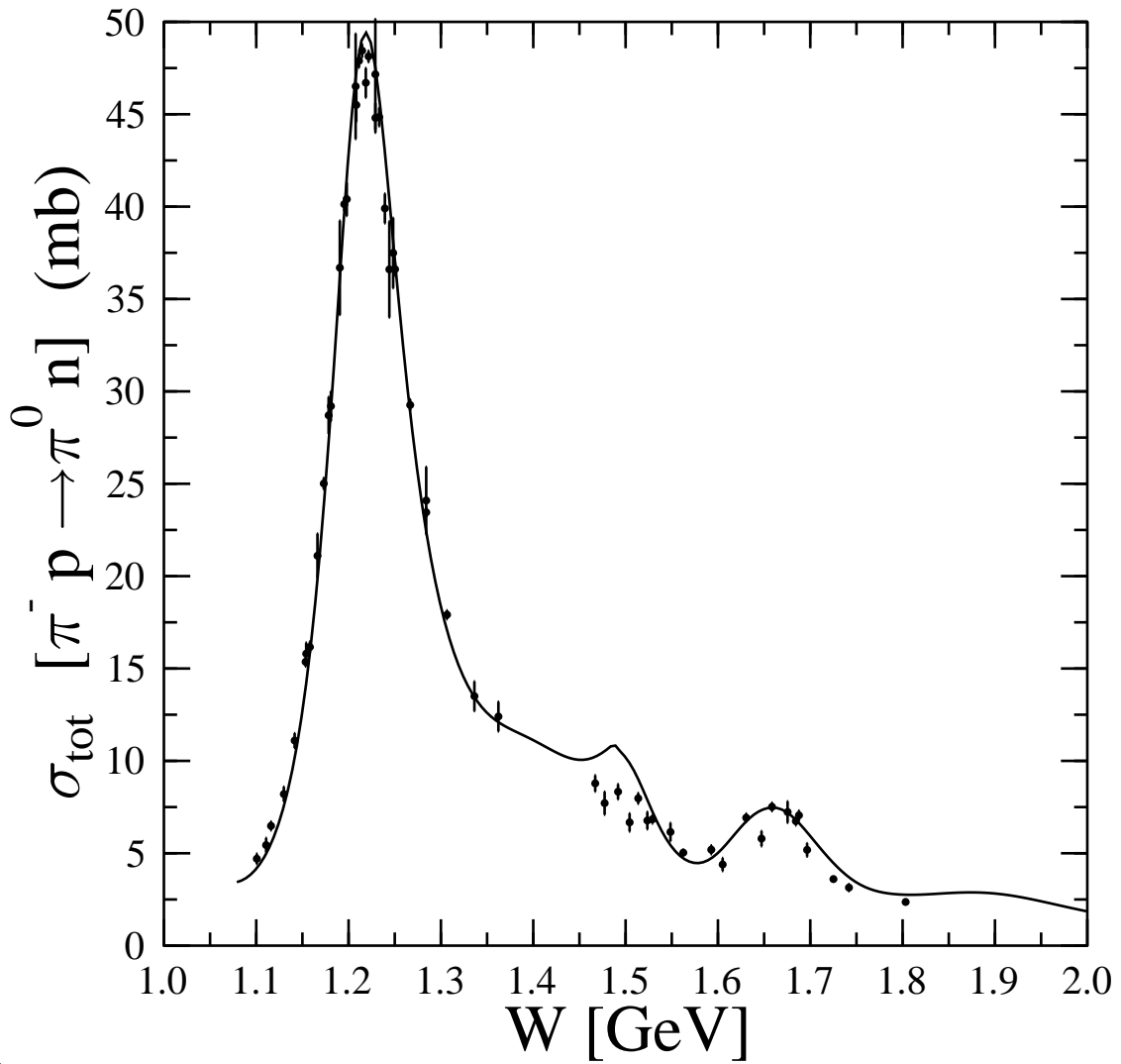


Fig 13

T.P. Vrana, S.A. Dytman, + T.-S. H. Lee

Baryon Resonance Extraction ...

This figure "fig14\_c.gif" is available in "gif" format from:

<http://arxiv.org/ps/nucl-th/9910012v2>

This figure "fig15\_c.gif" is available in "gif" format from:

<http://arxiv.org/ps/nucl-th/9910012v2>